Computational Modeling for Fate, Transport and Evolution of Energetic Metal Nanoparticles Grown via Aerosol Route

Dibyendu Mukherjee and Seyyed Ali Davari

Abstract Energetic nanomaterials have gained prominence in the development of solid-state propellants, explosives and pyrotechnics. Such interests stem from kinetically controlled ignition processes in nanoscale regimes resulting from larger specific surface areas, metastable structures and small diffusion length scales at fuel-oxidizer interfaces. To this end, numerous works have investigated the energetic properties of a large class of metal nanoparticles (NPs) that include Al, Si and Ti. Gas-phase synthesis of metal NPs involve rapid cooling of supersaturated metal vapor (monomers) that initiates free-energy-driven collisional process including condensation/evaporation, and finally, leads to nucleation and the birth of a stable critical cluster. This critical cluster subsequently grows via competing coagulation/coalescence processes while undergoing interfacial reactions including surface oxidation. A fundamental understanding of the thermodynamics and kinetics of these processes can enable precise controlling of the synthesis process parameters to tailor their sizes, morphology, composition and structure, which, in turn, tune their surface oxidation and, energetic properties. The complexity and extremely diverse time scales make experimental studies of these processes highly challenging. Thus, hi-fidelity computational tools and modeling techniques prove to be powerful for detailed mechanistic studies of these processes in an efficient and robust manner. The current chapter focuses on computational studies of fate, transport and evolution of metal NPs grown via aerosol routes. The chapter starts with the discussion on gas-phase homogeneous nucleation, and nucleation rates of critical clusters, followed by kinetic Monte-Carlo (KMC) based studies on non-isothermal coagulation/coalescence processes leading finally to the mass transport phenomena involving oxidation of fractal-like NPs.

Keywords Energetic nanomaterials · Metal nanoparticles · Kinetic Monte-Carlo simulation · Coagulation · Non-isothermal coalescence · Surface oxidation

D. Mukherjee (✉) · S.A. Davari
Nano-BioMaterials Laboratory for Energy, Energetics & Environment (nbml-E3),
Department of Mechanical, Aerospace & Biomedical Engineering,
University of Tennessee, Knoxville, USA
e-mail: dmukherj@utk.edu

M.K. Shukla et al. (eds.), *Energetic Materials*, Challenges and Advances
in Computational Chemistry and Physics 25, DOI 10.1007/978-3-319-59208-4_9

1 Introduction

1.1 Energetic Nanomaterials: A Broad Overview

The last few decades have seen a large volume of research work focus on a class of novel materials that demonstrate enhanced energetic property and reactivity thereby finding application in the development of propellants, explosives and pyrotechnics. To this end, past studies involving various forms of aluminized solid propellants prepared with different mixtures of aluminum powders and oxidizers as heterogeneous, composite solid propellants have indicated high burning rates and enhanced ignition [1–5]. The conventional wisdom in such mixtures calls for the stoichiometric mixing of the fuel and oxidizer to maximize their energy density. But, the overall kinetics of the process demands an atomistic mixture of the two components to minimize the fuel-oxidizer diffusion length during the reaction. Thus, for larger particle grain size, and hence lower interfacial area between the oxidizer and fuel, the overall reaction speed reflects mass-transfer limitations. On the other hand, a substantially larger surface area arising from fuel-oxidizer interfaces in nanoscale regime promote kinetically controlled ignition processes. This drive towards enhanced ignition kinetics has motivated extensive research on the development of nanosized oxidizer and fuel material that offer the potential (high surface area) for applications demanding rapid energy release. In this regard, increased research effort has been invested towards the use of nano-aluminum in explosives [5–8]. There has been notable work [9] analyzing the unique combustion properties of various energetic composite materials at nano-scale as compared to their properties at micro-scale. The application of various nano-powders and nano-composites of explosive materials like ammonium nitrite, cyclotrimethylene trinitramine (RDX), and aluminum in studying heterogeneous combustion characteristics [10] have also been carried out. In light of the aforementioned research drive towards novel energetic nanomaterials, rational design and synthesis of metal (fuel) nanoparticles with tailored size, morphology and compositions play a pivotal role in tuning the reactivity of these classes of nanomaterials with high accuracy. Nanomaterials are known to exhibit unique physico-chemical properties as compared to their bulk counterparts in different applications. The high specific surface areas of nanomaterials endow them with significantly enhanced surface reactivity as compared to their bulk counterparts. Atomic forces being effective approximately up to 5 interatomic distances, interfacial atoms with unsaturated bonds up to $\sim$1 nm in depth are highly reactive [11]. Moreover, usually the structures at these length scales are unbalanced and metastable due to their fast formation during manufacturing processes. Thus, while existing in their metastable state for long times under normal conditions, any perturbations sufficient enough for structural changes may result in the release of excess energy in the form of heat in an effort to relax to stable structural arrangements. Additionally, the diffusion length being exceedingly small in the nano-scale regime, the reaction rates are further increased by many orders of magnitude as compared to those the bulk state. These features have encouraged

researchers to investigate the enhanced energetic properties of a large class of metal nanoparticles. Traditionally, Aluminum (Al) with its large enthalpy of combustion ($\sim$1675 kJ/mol for bulk Al) has always been considered in the class of solid-state propellants and explosives [12]. But, considering that the enthalpy of combustion of an isolated Al atom is $\sim$2324 kJ/mol and the aforementioned interfacial energetic properties at nano-scale, nano-Al has been the center of attention in energetic nanomaterials. However, other fuels such as Si and Ti have also been studied by many researchers [13–15]. Thinner passivation layer, high flame temperature, and easy surface functionalizing are the advantages of Si. Numerous research works have also focused on elemental and structural variations of nanopowders to produce metastable intermolecular composites (MICs) [16–18]. Typically, MICs are constructed from nanosized reagents comprising fuels and oxidizers ideally mixed at atomic scale to reduce the diffusion paths between the two. While MICs stay stable under normal conditions, they are capable of interacting with each other under applied stimulations to release significant amount of energy [19]. Metal-metal oxide systems such as Al/Fe_2O_3, Al/Mo_3, Mg/CuO, etc. are examples of MICs. But, MICs are not limited to metal-oxide systems, since metal-metal systems such as Al/Ni, Al/Ti, B/Ti, etc. have also been studied rigorously. Moreover, studies have also investigated the role of different structures, and morphologies such as core shell [20], nanowires [21], nanoporous particles [22, 23], and multilayered nanofoils [24, 25] in the performance of MICs. To this end, manufacturing processes dictate much of the physical and chemical properties of nanoparticles and nanopowders such as shape, size distributions, elemental ratios, compositions, etc. Depending on the class (structure, composition) of nanomaterials that are required to be designed, different solution-phase and gas-phase synthesis techniques have been developed for the manufacturing of nanoparticles, and nanopowders. In relation to energetic metal NPs, one of the first methods proposed for production of nano-Al was based on the condensation of metal vapors generated by explosion of electrically induced wire [26]. This method is still widely used in the research community and nanopowders of many other elements have been produced by this technique [27, 28]. The mean particle sizes of the Al nanoparticles produced by this technique were in the 30–45 nm [29]. The other routes for the synthesis of energetic nanoparticles involve the chemical techniques. Sol-gel approach has been employed by researchers at Lawrence Livermore National Lab for the synthesis Al/Fe_2O_3 for the first time [30]. The process starts with polymerization of a solution containing precursors. The result is a dense three-dimensional cross-linked network. The energetic materials can be introduced during solution preparation or the gel stage of the process. Due to porous structure, the intimacy of the fuel-oxidizer components is significantly high. Specifically, lab-scale and industrial synthesis of metal nanoparticles typically employ rapid condensation of supersaturated metal vapor (monomer) that are generated from thermal evaporation of the bulk metal, electric arc discharge, laser ablation, flame reactors, plasma reactors, etc. During these gas-phase synthesis processes, rapid cooling ($\sim 10^3$–10^5 K/s) of the metal vapor initiates the saturated vapor to undergo the free-energy driven collisional process including condensation and evaporation, that finally leads to nucleation and the

birth of a stable cluster. This critical cluster subsequently grows via coagulation/coalescence and undergoes various interfacial reactions including surface oxidation. The thermodynamics and kinetics of each of the aforementioned events during the vapor-phase production of nanoparticles play significant role in tailoring their sizes, morphology, composition and structure, which, in turn, tune their extent of surface oxidation and hence, drive their energetic properties. The complexity of these processes combined with the extremely diverse time scales for the corresponding events during the vapor-phase evolution of nanoparticles makes it extremely challenging for a unified experimental study to capture the entire sequence of the fate, transport and growth of metal nanoparticles. To this end, the advent of hi-fidelity computational tools and modeling techniques provides a powerful advantage for the detailed mechanistic studies of these complex processes in an efficient and robust manner.

1.2 Modeling Work to Study Fate, Transport and Growth of Metal Nanoparticles

Numerous modeling studies have been developed over the years to investigate the vapor-phase synthesis of metal NPs. Generally speaking, these methods, and techniques can be broadly categorized into two different approaches. The first one involves the phenomenological models that approaches the problem based on macroscopic thermodynamic functions and solves the Smoluchowsky population balance equation by binning particle size domains into discrete sections and/or nodes to obtain size distributions in time, and space. In this direction, various sectional methods have been developed such as hybrid grid size [31], discrete-sectional [32, 33], and nodal methods [34]. Girshick et al. [35] studied the synthesis of Iron NPs in a plasma flame reactor using discrete-sectional method. Panda et al. [36] had developed very preliminary models for Al NP synthesis in aerosol flow reactors to show that low pressure, and temperature, and high cooling rate facilitate the formation of ultrafine NPs. Prakash et al. [37] developed a simple nodal model involving nucleation, surface growth, evaporation, and coagulation for synthesis of aluminum NPs. Mukherjee et al. [38] implemented a discrete-nodal model to account for size dependent surface tension in Al NPs. These methods are powerful, and robust to obtain the size distribution with low computation cost. However, they fail to capture the microscopic picture behind the chemical physics of the processes. Moreover, in general they suffer from significant numerical diffusion, which brings in numerical artifacts in the concentrations and particle size distribution data.

The second approach involves molecular level models, wherein Molecular Dynamics (MD) and Monte Carlo (MC) simulations are used to estimate the structural and free energy variations as well as the source terms resulting from nucleation process from the first principles. In classical MD, an initial position and

momentum is assigned for each atom/molecule, and then Newton's law is applied to molecules. An intermolecular potential is allocated to the system, and trajectories of molecules are traced in order to identify phase transition and nucleation rate. Zachariah et al. [39] used a MD simulation to validate their sintering model, and showed coalescence time is size dependent for solid particles. Yasuoka et al. [40] calculated the nucleation rate for Ar and showed that surface excess energy and entropy takes bulk value for clusters above 50. Lummen et al. [41] investigated homogenous nucleation of Platinum nanoparticles from vapor phase and extracted the nucleation rate and properties of critical cluster. While MD is a powerful technique for molecular scale simulation, it is limited to small time scale simulations. The typical time step required for a MD simulation is in the order of ~ 1 fs. Therefore, in order to accomplish a 1 s simulation, 10^{14} time steps are required, which is computationally expensive and beyond the typical machines capacity. Monte Carlo is a stochastic technique in which a random configuration is identified at each step, and system decides to accept or reject the configuration randomly. The fate of the system is determined through the random jumps in configurations. The simulation can be carried out to obtain the system free energy [42], structure of nanoparticles [43], evolution of size distribution [44] etc. Gillespie [45] developed a stochastic model for growth process and coalescence. Liffmann [46] developed a model for coagulation of particles to solve the Smoluchowski equation, and introduced a topping up method to account for particle loss during the simulation. Kruis et al. [47] developed a MC model for nucleation, surface growth, and coagulation and compared their results with analytical solutions. Mukherjee et al. [44] considered the effect of coalescence heat release during particles collision and formation for Silicon and Titania nanoparticles. Efendiev et al. [48] applied a hybrid MC simulation to the growth of SiO_2/Fe_2O_3 binary aerosol. Mukherjee et al. [49] developed a collision-coalescence model to study the effect of fractal morphology on surface oxidation of Aluminum (Al) nanoparticles.

In this chapter, we mainly focus on the KMC-based models to investigate the growth and evolution of metal nanoparticles synthesized as energetic nanomaterials via aerosol routes. The following sections in this chapter would develop into the various MC-based models that we have developed in capturing the detailed chemical-physics behind the formation of these particles that include processes such as nucleation, surface growth, coagulation, coalescence, and finally, their effects in driving the surface oxidation of metal nanoparticles. We consider each of the processes separately, starting with the earliest stage of nucleation, and tracing them up to coagulation/coalescence and finally, surface oxidation (see Fig. 1). The goal here is to provide a mechanistic study of each of these processes that can lead to a fundamental understanding on the role of these processes in tailoring the sizes, morphologies and extents of oxidation and hence, driving the energetic behavior of passivated metal or spent metal-oxide nanoparticles as shown by the schematics in Fig. 1.

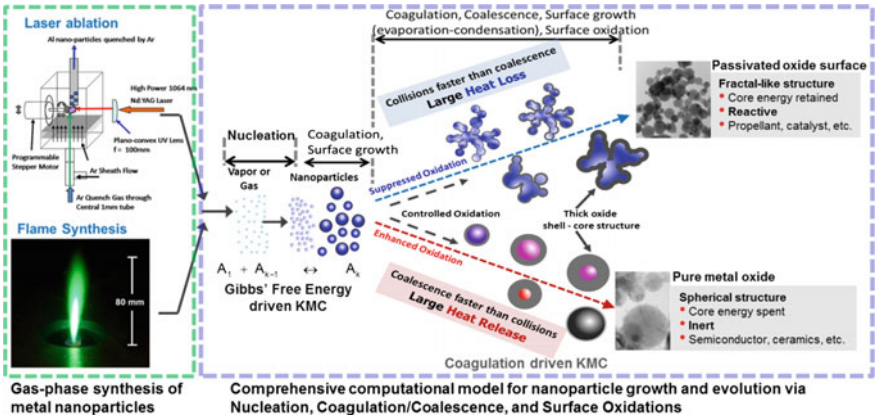

Fig. 1 Schematic representation of computational models studying the fate of metal nanoparticles grown and evolved from gas-phase synthesis via nucleation, coagulation/coalescence, and surface oxidation

2 Homogeneous Gas-Phase Nucleation of Metal Nanoparticles

Generally, nucleation can be realized as a first-order phase transition that marks the birth of a thermodynamically stable condensed phase in the form of a critical nucleus and is the precursor to the crystallization process, followed by subsequent growth of the critical cluster via coagulation and condensation/evaporation processes. In formation of particles, nucleation is the first physical process that occurs during system evolution. Based on existence of a foreign material, nucleation can be subcategorized into homogeneous, and heterogeneous nucleation. Atoms and molecules need nucleation sites in order to condense on the sites and create a new phase. The nucleation sites can be provided by the nucleating atoms, and molecules (self-nucleation) or by another material or surface. Homogeneous nucleation is defined as nucleation of specific phase of a material (vapor e.g.) on an embryos comprised of that material, while foreign materials do not play any role in terms of providing nucleation site in the process. On the other hand, heterogeneous nucleation is the nucleation of specific phase of a material (vapor e.g.) on an embryos comprised of another material. Homogeneous nucleation is a kinetically disfavored process that involves surmounting a nucleation barrier during the vapor-phase cooling of monomers leading to supersaturation where in clusters grow via collisions and/or condensation of monomers, or decompose into smaller clusters and monomers via evaporation. The aforementioned processes continue till the critical nucleus is formed as the new phase that resides on top of the nucleation barrier and undergoes barrier-less spontaneous growth under any perturbation. The presence of a free energy barrier in a first-order phase transition process makes nucleation a rare event whose exceedingly small length and time scales pose an insurmountable

challenge for designing experiments that can accurately monitor and/or control the in situ NP formation [50–52]. Homogeneous nucleation can occur in presence of supersaturated vapor phase. The extent of supersaturation of a material in a carrier gas at temperature T is determined by saturation ratio, which is defined as:

$$S = \frac{n_1}{n_s(T)} = \frac{p_1}{p_s(T)} \tag{1}$$

in which n_1, and p_1 are monomer concentration, and pressure respectively, and n_s, p_s are saturation monomer concentration, and pressure at temperature T. $S < 1$ indicates a relaxed system, $S = 1$ a saturated system (equilibrium), and $S > 1$ indicates a supersaturated system (tense). Sudden cooling down is a very common method for creating a supersaturated system during gas-phase synthesis of nanoparticles via aerosol routes. A sharp temperature gradient $\sim 10^3$–10^6 K/s is required for transition to supersaturation by sudden cooling. These types of temperature gradients can be provided by plasma ablation, thermal evaporation, and flame synthesis with precursors and subsequent cooling in a reactor cell for particle generation. The formation of particles occurs in two stages, the first being nucleation and the emergence of critical nucleus (or, critical cluster), and the second is the growth of the critical nucleus. During nucleation process the change in enthalpy is negative ($\Delta H < 0$), which is thermodynamically favorable. However, the change in entropy is negative as well ($\Delta S < 0$), thereby causing a competition between the two thermodynamic quantities. Usually there is an energy barrier in the first stage to be surmounted before the critical nucleus is formed. Figure 2 shows the typical Gibbs' free energy barrier as a function of cluster sizes that is encountered during the nucleation process. The Gibbs' free energy of formation increases up to a critical cluster size corresponding to the critical nucleus or cluster beyond which the formation energy decreases with size. The height of the free energy at the critical cluster size is called nucleation barrier that dictates the driving force behind nucleation and particle formation. The change in the free energy during a formation reaction is positive for clusters smaller than critical cluster (unfavorable), and after the critical cluster size, the change is negative (favorable). The process starts with monomer collisions. These collisions lead to small cluster formations that can, in turn, collide with each other or other monomers (condensation) to grow into larger clusters, and dissociate due to evaporation into smaller clusters. The cluster growth, and dissociation continue until a sufficiently large cluster size emerges and passes the nucleation barrier. The rate at which clusters pass the nucleation barrier is called nucleation rate. Beyond this critical stage, the free energy change for cluster formations being favorable, clusters that pass the barrier grow spontaneously resulting in rapid surface growth. The driving force at this stage is the difference between monomer concentration (n_1) and saturation monomer concentration over a particle ($n_{s,i}$) that is determined by the Kelvin relation:

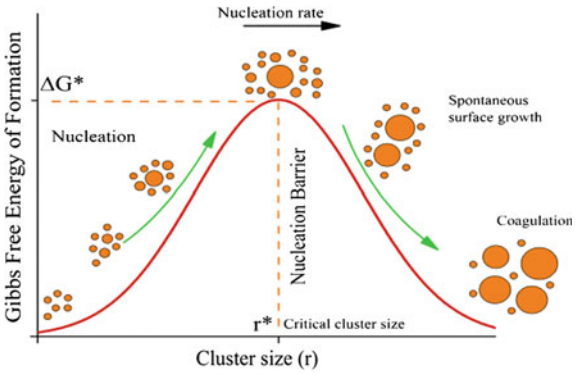

Fig. 2 Typical Gibbs free energy of formation, and nucleation barrier. Condensation and evaporation occur on *left side* of the barrier until the nucleation onset at the top of the barrier, followed by spontaneous surface growth and coagulation

$$n_{s,i} = n_s \exp\left(\frac{4\sigma v_1}{d_i k_B T}\right) \tag{2}$$

in this equation n_s is saturation monomer concentration, σ surface tension, v_1 monomer volume, d_i diameter of the particle, T temperature, and k_B the Boltzmann constant. The monomer concentration greater than saturated monomer concentration over the particle ($n_1 > n_{s,i}$) drives condensation on the particle whereas the reverse ($n_{s,i} > n_1$) drives evaporation from the particle causing them to shrink via monomer loss. The surface growth continues until the equilibration of monomer concentration and saturated monomer concentration over particles ($n_{s,i} = n_1$) wherein coagulation and subsequent coalescence becomes the dominant process for the particle growth and evolution.

However, the presence of a free energy barrier in the aforementioned first-order phase transition process makes nucleation a rare event whose exceedingly small length and time scales pose an insurmountable challenge for designing experiments that can accurately monitor and/or control the in situ NP formation [50–52]. Hence hi-fidelity simulations that capture the mechanistic, detailed and yet, collective picture of vapor-phase homogenous nucleation, through systemic modeling of the chemical physics of the problem, become necessary for predictive synthesis of tailored metal NPs. Here one needs to note that most homogenous vapor-phase nucleation studies (specifically, for non-polar liquids and small organic molecules) [35, 53–57] in the past have resorted to the Classical Nucleation Theory (CNT) framework due to its ability to provide a robust yet, relatively accurate investigation into the basic chemical physics of nucleation in a convenient and elegant fashion. Thus, in the next sub-section we present a brief introduction to the basic premises of the CNT.

2.1 Classical Nucleation Theory (CNT)

The reaction kinetics for the aforementioned processes can be represented as:

$$\begin{gathered} M + M \leftrightarrow M_2 \\ M + M_2 \leftrightarrow M_3 \\ M + M_3 \leftrightarrow M_4 \\ \ldots. \\ M + M_i \leftrightarrow M_{i+1} \\ \ldots. \end{gathered}$$

where M_i denotes a cluster containing i number of monomers (called i-mer). It describes a set of coupled reactions. Note that the set of reactions above does not include cluster-cluster collisions. Since the concentration of clusters in compare to monomer is relatively low, this type of collisions can be neglected. In order to investigate the kinetics behind the set of reactions, one needs to know the rate of reaction in forward, and backward direction. In the free molecular regime of kinetic theory, when clusters are smaller than the mean free path of the gas, the rate at which two clusters collide each other can be written as:

$$K_{ij}^{F} = K^{F}(V_i, V_j) = \left(\frac{3}{4\pi}\right)^{\frac{1}{6}} \left(\frac{6k_B T_p}{\rho_p}\right)^{\frac{1}{2}} \left(\frac{1}{V_i} + \frac{1}{V_j}\right)^{\frac{1}{2}} \left(V_i^{1/3} + V_j^{1/3}\right)^2 \tag{3}$$

K_{ij}^{F} collision kernel in free molecular regime, is the number of collisions between two clusters containing i, and j number of monomers per unit of time, k_B Boltzmann constant, ρ_M clusters density, and T_i, and v_i are temperature and volume of each cluster respectively. The backward rate is determined based on the principle of detailed balance (or microscopic reversibility) requiring the transition between two states to occur at the same rate at equilibrium. Thus, for the generalized reaction for the formation of an i-mer:

$$M + M_{i-1} \leftrightarrow M_i$$

The rate of change of concentration for (i-1)-mer can be written as:

$$\frac{dn_{i-1}}{dt} = -k_{f,i-1} n_1 n_{i-1} + k_{b,i} n_i \tag{4}$$

where $k_{f,i-1}$ and $k_{b,i}$ are the forward and backward reaction rate respectively, and n_i is concentration of i-mer where under the assumption of all successful collisions in the system, $k_{f,i-1} = K_{i-1,1}^{F}$. Since the process is at the equilibrium:

$$\frac{dn_{i-1}}{dt} = 0 \rightarrow k_{f,i-1} n_1 n_{i-1} = k_{b,i} n_i \tag{5}$$

Reaction constant, K_c, is defined as:

$$K_c = \frac{k_{f,i-1}}{k_{b,i}} = \frac{n_i}{n_1 n_{i-1}} \tag{6}$$

Also, from thermodynamics, reaction equilibrium constant can be expanded as:

$$K_p = \frac{p_i/p_0}{p_{i-1}/p_0 \; p_1/p_0} = \exp\left(-\frac{\Delta G_{i,i-1}}{k_B T}\right) = K_c n_0 \tag{7}$$

where p_i, and $\Delta G_{i,i-1}$ are partial pressure of i-mer, and Gibbs free energy change for the forward reaction. Subscript "0" refers to the reference pressure, and concentration.

Therefore, the backward rate can be written as:

$$k_{b,i} = k_{f,i-1} n_0 \exp\left(+\frac{\Delta G_{i,i-1}}{k_B T}\right) \tag{8}$$

In order to evaluate the k_b, we need to know the Gibbs free energy change for the forward reaction, $\Delta G_{i,i-1}$.

Considering a particle in equilibrium with its vapor, and realizing that volume per atom in gas phase is greater than the particle phase ($v_{1,v} \gg v_{1,p}$), and assuming the vapor phase behaves as an ideal gas, the difference in chemical potential of particle (μ_p) and gas phase (μ_v) can be related through the Kelvin relation as:

$$\mu_v - \mu_p = \frac{2\sigma v_{1,p}}{r} = k_B T \ln\left(\frac{p(r)}{p_s}\right) = k_B T \ln(S) \tag{9}$$

where r is the radius of the particle, σ is the surface tension in the bulk regime, and p(r) is monomer vapor pressure over the particle. Based on the change in chemical potential at gas, and particle phase, the Gibbs free energy of formation of an i-mer from its vapor can be written as:

$$\Delta G_i = 4\pi\sigma r^2 - i k_B T \ln(S) \tag{10}$$

The first term in (10) represents the change in energy due to phase change. The second term shows the increase in energy due to formation of surface. The Gibbs free energy of formation is a function of size, temperature and saturation ratio of the system. For a specific saturation ratio above 1 ($S > 1$), the ΔG_i has maxima. Differentiating with respect to size, and equating to zero:

$$r^* = \frac{2\sigma v_{1,p}}{k_B T \ln(S)} \tag{11}$$

For cluster smaller than r* the Gibbs free energy of formation increases with size, and after that it decrease with size. The r* represents the radius of critical cluster. The Gibbs free energy of formation at this size represents the nucleation barrier, and can be written as:

$$\Delta G^* = \frac{16\pi}{3} \frac{v_{1,p}^2 \sigma^3}{(k_B T \ln(S))^2} \tag{12}$$

Analyzing (11) and (12), the critical cluster size, and nucleation barrier are reduced as the saturation ratio increases. Defining the dimensionless surface tension as:

$$\theta \equiv (36\pi)^{1/3} \frac{\sigma v_{1,p}^{2/3}}{k_B T} \tag{13}$$

thus, (10) can be rearranged as:

$$\frac{\Delta G_i}{k_B T} = \theta i^{2/3} - i \ln(S) \tag{14}$$

This equation relates the dimensionless Gibbs free energy of formation to the dimensionless surface tension, saturation ratio, and cluster size. The equilibrium concentration of clusters can be expressed as:

$$n_i^e = n_1 \exp\left(-\frac{\Delta G_i}{k_B T}\right) \tag{15}$$

Using the CNT expression for clusters formation energy, the equilibrium concentration becomes:

$$n_i^e = n_1 \exp\left(-\theta i^{2/3} + i \ln(S)\right) \tag{16}$$

examining (16), we realize by substituting $i = 1$, $n_1^e \neq n_1$, which clearly is incorrect. Moreover, one can observe that ΔG_i when $i = 1$ gives a nonzero value, while it is expected that the Gibbs free energy of formation for monomer be zero. So far, the obtained Gibbs free energy of formation showed inconsistencies in terms of monomer concentration, and formation energy. However, the greatest advantage of classical nucleation theory, namely simplicity, motivated researchers to adjust the Gibbs

free energy of formation to solve the inconsistency problem. Girshick et al. [35] suggested to replace $i^{2/3}$ with $(i^{2/3} - 1)$ to solve inconsistency in monomer concentration and Gibbs free energy of formation. The self-consistent form is written as:

$$\frac{\Delta G_i}{k_B T} = \theta\left(i^{2/3} - 1\right) - (i - 1)\ln(S) \tag{17}$$

Note the equilibrium concentration of clusters decreases with increase of size up to critical cluster. After that increasing the size shows increase in concentration, which physically is incorrect. Thus, the derived equilibrium concentration is valid only up to $i = i^*$.

Now going back to the set of coupled equation, we can write the change in concentration for an i-mer as:

$$\begin{aligned} &M + M_{i-1} \leftrightarrow M_i + M \leftrightarrow M_{i+1} \\ &\frac{dn_i}{dt} = \left(k_{f,i-1} n_1 n_{i-1} - k_{b,i} n_i\right) - \left(k_{f,i} n_1 n_i - k_{b,i+1} n_{i+1}\right) \end{aligned} \tag{18}$$

It has been assumed that the only involved mechanisms that change the concentration of a cluster are condensation and evaporation. Since the concentration of clusters is significantly lower than monomers, collisions between clusters can be neglected. However, at high saturation ratios, where the concentration of clusters is considerable, this assumption becomes questionable. The first term in the RHS represents the ingoing flux to the i-mer, and the second term in the RHS represents outgoing flux from the i-mer. The nucleation current for each cluster, J_i, is defined as:

$$J_i = k_{f,i-1} n_1 n_{i-1} - k_{b,i} n_i \tag{19}$$

Therefore the rate of change in concentration for i-mer can be written in terms of nucleation current as:

$$\frac{dn_i}{dt} = J_i - J_{i+1} \tag{20}$$

It is usual to define a steady state for the all clusters in the system. In the steady state the concentration does not change in time and the income current and outgoing current are equal to steady state nucleation current, J_{ss}:

$$\frac{dn_i}{dt} = 0 \rightarrow J_i = J_{i+1} = J_{ss} \tag{21}$$

J_{ss} is called steady state nucleation rate, which can be derived as:

$$J_{ss} = \frac{n_1^2}{\sum_{i=1}^{i=M} \frac{1}{k_{f,i} \exp\left(-\frac{\Delta G_i}{k_B T}\right)}} \tag{22}$$

The steady state nucleation rate is related to the monomer concentration and Gibbs free energy of formation of clusters. If the number of terms in the summation is sufficiently large, then the summation can be replaced by integral. After a little mathematical manipulation the steady state nucleation obtained as:

$$J_{ss} = \frac{d_1^2}{6}\sqrt{\frac{2k_B T\theta}{m_1}}\frac{n_1^2}{S}\exp[\theta - \frac{4\theta^3}{27(\ln(S))^2}] \tag{23}$$

where d_1, and m_1 are the diameter and mass of monomer respectively. It can be observed, as the nucleation rate is a steep function of saturation ratio.

2.2 *Modeling Nucleation: KMC Based Model and Deviations from CNT*

Enormous numbers of studies have been carried out to verify the nucleation rates from classical nucleation theory. Generally speaking, the experimental set-ups for these studies comprise adiabatic expansion chamber [58, 59], upward diffusion chamber [54], laminar flow chamber [60, 61], turbulent mixing chamber [62, 63], etc. The main difference between these methods is how the supersaturated system is generated. Interestingly, the results for comparisons between nucleation rates from classical nucleation theory and experiments range from excellent agreement up to several order of magnitude differences. Wagner et al. [59] used an adiabatic expansion approach and studied nucleation rates of water and 1-propanol, and observed that classical nucleation theory over predicts the nucleation rate for water, while the measured nucleation rates for 1-propanol was considerably higher than what classical nucleation theory predicts (see Fig. 3). The discrepancies between measured nucleation rates and classical nucleation predictions become even more severe in the cases of metal vapors [64, 65]. To this end, Zhang et al. had carried out a comprehensive review on the topic [66].

The discrepancies between theory and experimental studies can be possibly explained in light of the fundamental assumptions made in the classical nucleation theory. It can be observed that the nucleation rate bears an exponential dependence on the Gibbs free energy of formation of clusters. Thus, any error in the Gibbs free energy of formation can change the nucleation rate drastically. To this end, the most significant assumption is introduced when the bulk properties are extended to the

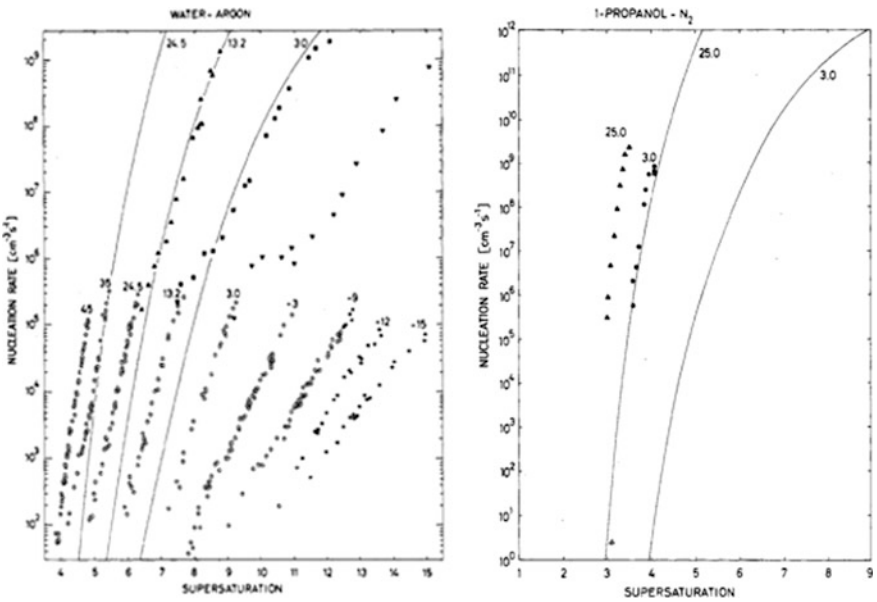

Fig. 3 Nucleation measurement of water and 1-propanol at different initial chamber temperature for different saturation ratio. Curves are predicted values from CNT (Adapted with permission from *J. Phys. Chem., 1981, 85 (18), 2694*. Copyright (1981) American Chemical Society)

smaller cluster sizes. The thermophysical properties of the bulk phase vary significantly from those for the nanophase materials. Previous studies have shown that material properties change as a function of size [67, 68]. Thus, Mukherjee et al. [38] had employed a size-dependent surface tension in their nucleation study that had resulted in the Gibbs free energy of formation for different cluster sizes to indicate multiple peak profiles. In the aforesaid study, the implementation of a size-dependent surface tension (non-capillarity approximation) in a hybrid nodal model had resulted in an earlier onset of nucleation than that predicted from classical nucleation theory (Fig. 4). The other questionable assumption lies in the morphology of the clusters. CNT assumes spherical cluster shapes. However, at the atomistic level, the geometry of a cluster with few atoms is barely spherical and hence, other geometric and electronic arrangements can generate lower energy structure that are more stable. Such structural stability of certain localized cluster sizes can possibly explain the existence of some cluster sizes with relatively higher concentrations as compared to those for their neighboring cluster sizes in experimental observations [69, 70]. In some literatures, these cluster sizes have been referred to as magic numbers. Furthermore, Li et al. [42, 71, 72] had also calculated the Gibbs free energy changes, and association rate constants using MC configuration integral and atomistic (MD) simulations, and showed that the Gibbs free energy of formation for Al clusters is different than what classical nucleation theory predicts (Fig. 5). Specifically, this work had explained the differences in the

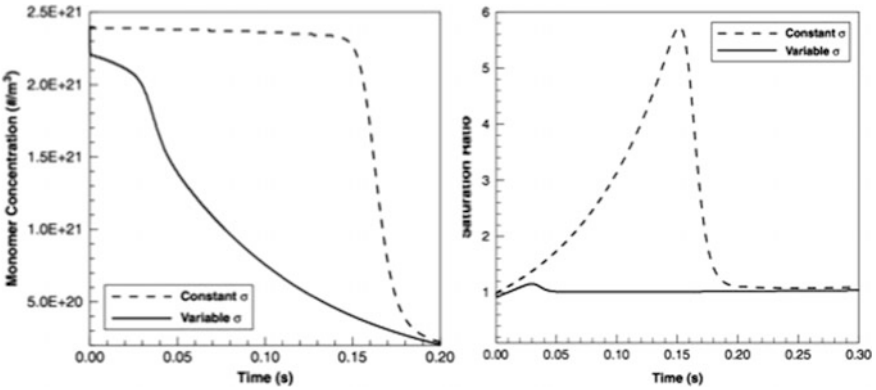

Fig. 4 Difference in onset of nucleation for constant and size-dependent surface tension. Sudden changes in monomer concentration and saturation ratio illustrate the onset of nucleation (Reprinted from *J. Aerosol Sci., 37, 1388 (2006)*. [38] Copyright (2006), with permission from Elsevier)

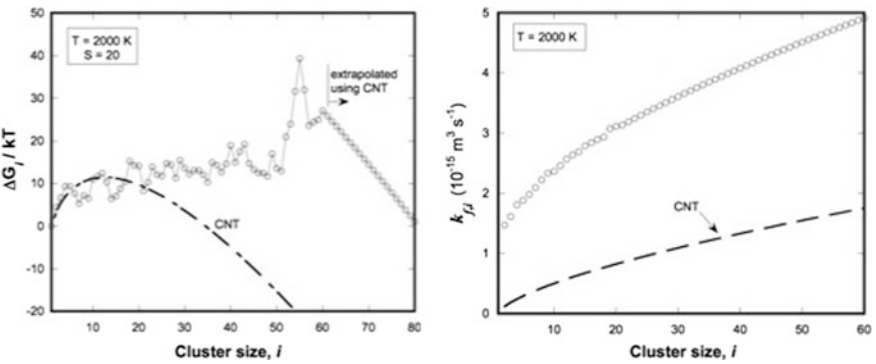

Fig. 5 Comparison between classical nucleation theory, and MC, MD simulations for Gibbs free energy and forward reaction rate of aluminum clusters considering structure of clusters (Reprinted from *J. Chem. Phys. 131, 134,305 (2009)* [72] with the permission of AIP Publishing)

forward reaction rates based on the open-shell structures of Al atoms in the clusters as compared to the conventional spherical assumptions in classical nucleation theory. One of the widely accepted outcomes of CNT-based studies is the derivation of the unified nucleation flux based on the inherent steady-state assumptions of cluster concentration invariance over relatively short period of time during cluster growth. To this end, MD studies by Yasuoka et al. [40] had observed that the steady-state nucleation rates are valid only for clusters above a certain size wherein the nucleation rate was found to be constant and size independent. However, it was noted that the clusters below that size do not reach steady-state and their concentrations change in time. Specifically, cluster concentrations decrease as cluster size increases up to a certain size beyond which the concentrations become

approximately invariant with size. Finally, beyond the aforesaid broad assumptions, CNT also assumes that all clusters and background gases are at the same temperature, thereby assuming the occurrence of an isothermal nucleation event. But, in order for isothermal nucleation to be established the pressure of background gas must be sufficiently high that results in the condensable vapor being dilute as compared to the background gas, thereby allowing the heat of condensation to be rapidly quenched by collisions with the background gas molecules. However, at high saturation ratio this assumption becomes questionable. Wyslouzil et al. [73] had investigated the effect of non-isothermal nucleation on the nucleation rate of water that revealed at low pressure conditions, non-isothermal nucleation rate is significantly lower than the isothermal counterpart and as background gas pressure increases, this difference is reduced. Similar behaviors were also observed by Barrett [74] for the nucleation studies carried out on Argon, *n*-butanol, and water. These results are represented in the nucleation rate plots in Fig. 6 for water (left) and Argon (right) under different background gas pressure conditions.

To address and fundamentally investigate the aforementioned discrepancies in nucleation studies, one requires more realistic models that can facilitate easy elimination of the aforesaid assumptions while capturing the ensemble physics of cluster growth and nucleation. Such robust models can provide deep physical understanding of the mechanistic picture behind nucleation. To this end, one would consider MD simulations as the first choice. However, as mentioned earlier, they are severely restricted by the time steps, and are not practical for analyzing ensemble processes that occur over vastly varying time scale ranges. Thus, stochastic-based KMC models with rate-controlled time steps become the preferred simulation technique that can capture an ensemble, statistically random and rare

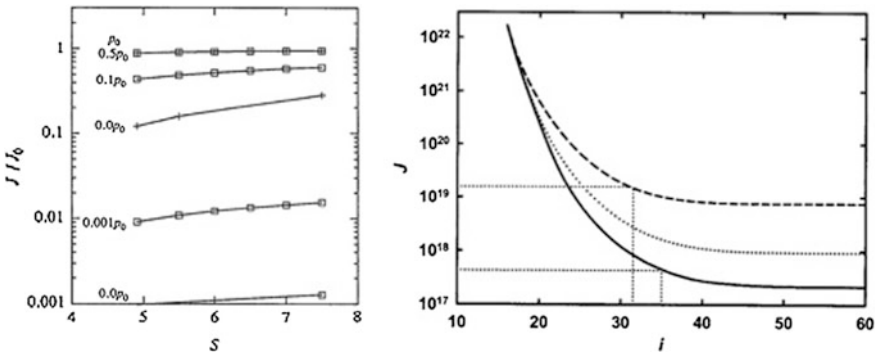

Fig. 6 Comparisons of isothermal, and nonisothermal nucleation rates. *Left* effect of pressure on the nucleation rate and comparison with classical nucleation theory for water as a function of saturation ratio, and background pressure [Reprinted from *J. Chem. Phys. 97, 2661 (1992)* [72] with the permission of AIP Publishing]. *Right* effect of background gas on the nucleation rate of Argon, (*dashed line*) classical nucleation theory, (*solid line*) absence of background gas, and (*dotted line*) low background gas (Reprinted from *J. Chem. Phys. 128, 164519 (2008)* [73] with the permission of AIP Publishing)

event like nucleation. Additionally, the simple yet elegant algorithm of MC models allows for easy implementation of additional physics without a priori assumptions been made.

As mentioned earlier, KMC models can provide realistic simulations to capture physico-chemical phenomena in a kinetically driven time step. They can solve multi-scale and multi-time systems without requiring any governing equation. Generally, the KMC models can be divided into two broad categories, constant-number, and constant-volume. The constant-number models keep the number of particles in the simulation box constant, and whenever a successful event is identified which changes the number of particles (e.g. coagulation, evaporation), the system needs to either add or remove a particle from the simulation. The other category is constant-volume methods. Usually, these methods can be divided into "time-driven" [75, 76], and "event-driven" [47, 77, 78] models. In the time-driven technique the time step is determined before the simulation, and based on the time step, system decides how many events, and which events become successful events. In the "event-driven" technique, first an event is identified, then an appropriate time step based on the rate of the identified event is calculated. The probability of the event should be related to the rate of event.

At each time step two clusters are chosen for the growth process. In the system of reactions (R1) the forward rate of reaction is based on the collision kernel in the free molecular regime. Therefore, the probability of the event can be written as:

$$p_{i,j} = \frac{k_{i,j}}{\sum_{i,j} k_{i,j}} \tag{24}$$

Summation over all possible kernels can be an expensive computational task. Instead, Matsoukas et al. [78] showed that the summation over all pairs can be replaced by the maximum kernel among particles without sacrificing the accuracy significantly.

$$p_{i,j} = \frac{k_{i,j}}{k_{max}} \tag{25}$$

The time step corresponds to the event then can be calculated based on the total number of particles in the simulation box, the volume of the simulation box, and the rate of events as:

$$\Delta T_f = \frac{V_{comp}}{\sum R_f} = \frac{V_{comp}}{\sum k_{i,j}} = \frac{2V_{comp}}{\langle k_{i,j} \rangle M(M-1)} \tag{26}$$

where, V_{comp} represents the volume of the simulation box, and $\langle k_{i,j} \rangle$ is the mean kernel of the system. The factor of "2" was introduced to prevent double counting of collision pairs. Calculating the mean kernel can be computationally expensive. Studies [44, 79] showed that one can replace the mean kernel by the kernel of the

identified kernel without introducing significant error in the results. The same logic can be implemented for the backward events such as evaporation. Growth and decomposition processes will change the total number of particles in the simulation. It has been shown [46] that the accuracy of MC simulation is proportional to $1/\sqrt{N}$, where N is the total number of particles in the simulation box. Therefore, in order to preserve the accuracy, whenever the total number of particles drops to half of the initial value, the entire simulation box is duplicated [46].

Recently, we have been actively involved with the development of a hi-fidelity KMC model to study the homogeneous nucleation of Al nanoparticles from vapor phase. [80] The model uses the self-consistent expression for the Gibbs free energy of formation as expressed in Eq. 17. To this end, based on the fundamental principles of Metropolis algorithm and detailed balancing, one can model the basic probabilities of condensation and evaporation during the cluster growth processes based on the Gibbs free energy changes during the reactions as:

$$P_c = \begin{cases} e^{-\frac{\Delta G_{i,i-1}}{k_B T}} & \Delta G_{i,i-1} > 0 \\ 1 & \Delta G_{i,i-1} \leq 0 \end{cases} \tag{27}$$

$$P_e = \begin{cases} 1 & \Delta G_{i,i-1} > 0 \\ e^{-\frac{\Delta G_{i,i-1}}{k_B T}} & \Delta G_{i,i-1} \leq 0 \end{cases} \tag{28}$$

Our current approach for the simulations involves modeling the cluster-cluster collisions based on the probability given by Eq. 25. On the other hand, Eqs. 27 and 28 aim to drive the process in presence of a nucleation barrier, wherein the probability of condensation is hindered by the change in the Gibbs free energy during condensation, while the probability of evaporation is unity. The rationale behind the model development is that the particles are driven by the free energy profile until they surmount and eventually, pass the nucleation barrier to form the critical cluster sizes. Once the critical clusters pass the barrier, their growth by condensation is favored ($p_c = 1$), while their evaporation is not favored anymore ($p_e < 1$). Preliminary results from our aforesaid KMC simulations indicate the nucleation rates to deviate from the steady-state values CNT prediction. [80] Specifically, smaller clusters (<10-mer size in Fig. 7) indicate higher nucleation rates as compared to larger clusters all the way up to the critical cluster size that finally attain a steady state constant flux at the onset of nucleation (Fig. 7). Such observations were also reported in previous MD simulations on vapor-phase nucleation of a Lennard-Jones fluid [40]. These results indicate that our KMC models can eliminate a priori CNT assumptions, while being not limited to the typical MD time steps. In doing so, one can envision a realistic nucleation model in future that can facilitate the elimination of all built in assumptions of CNT while accounting for other physical effects such as size-dependent properties and the effect of heat of condensation. This is an ongoing

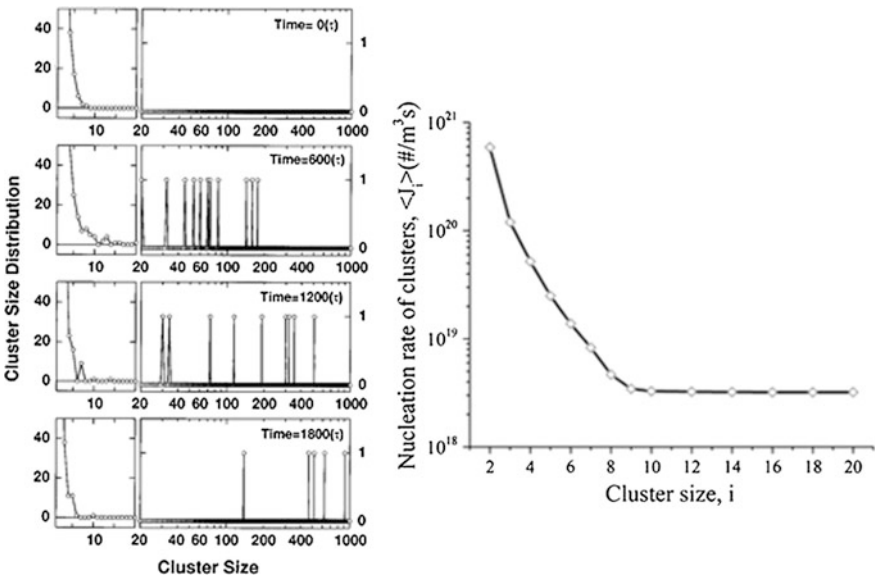

Fig. 7 Cluster distribution and nucleation rate based on: *Left* MD simulations for nucleation of Lennard-Jones fluid, (Reprinted from *J. Chem. Phys. 109, 8451 (1998)* [40] with the permission of AIP Publishing) and *Right* Our KMC simulation of Aluminum nanoparticle formation from vapor phase

research effort with the authors' groups that can eventually lead to fundamental understanding and hence, hitherto elusive comparisons with experimental results for nucleation process of metal nanoparticles.

3 Non-isothermal Coagulation and Coalescence

Coagulation refers to the growth mechanism of nanoparticles via collisional agglomeration that typically ensues following the nucleation of the critical cluster when the particles undergo barrier-less spontaneous growth during gas-phase synthesis. Coagulation is frequently followed by coalescence resulting in structural re-arrangements leading to surface area/energy reductions, and neck formations in the sintered aggregates. Here, "*agglomerates*" refer to an assembly of primary particles (i.e., physically joined together) whose total surface area does not differ appreciable from the sum of specific surface areas of primary particles, whereas "*aggregates*" refer to an assembly of primary particles that have grown together to form necks via sintering/re-arrangements whose total specific surface area is less than the sum of the surface areas of the primary particles. The study of coagulation and coalescence of nano-sized aerosols resulting in aggregate/agglomerate formation and the growth characteristics, morphology and size distributions of primary

particles in the aggregates/agglomerates have been an area of extensive study in both theoretical and experimental works. Coalescence of particles resulting in spherical particles can be of importance in predicting uniformity of particle sizes required for pigment synthesis, chemical vapor deposition, carbon black, etc. On the other hand, clusters of individual primary particles forming agglomerates of higher specific surface area are known to enhance catalytic activity [81] or the rate of energy release in propellants [82]. Indeed many thermal, mechanical and optical properties [83] are determined by the size of primary particles. Thus, the ability to predict and control primary particle sizes of nano-structured materials either in the free-state or stabilized in an aggregate or agglomerate is of paramount importance in the implementation of many of the engineering applications of nanomaterials that envisage a size dependent property, including energetic behavior of metal nanoparticles.

During many gas-phase aerosol processes, a high concentration of very small particles undergoes rapid coagulation. This may lead to the formation of fractal-like agglomerates consisting of a large number of spherical primary particles of approximately uniform diameter [84]. The size of the primary particles ultimately is determined by the relative rates of particle-particle collision and coalescence of a growing aerosol [85]. At very high temperatures, for example, particle coalescence occurs almost instantly on contact resulting in uniform spherical primary particles of relatively small surface area. At low temperatures, the rate of coalescence may be so slow that particles undergo many frequent collisions before the agglomerate can undergo structural re-arrangements, leading to fractal-like agglomerates consisting of very small primary particles, and thus larger surface area. Of particular interest are those intermediate conditions where neither process is rate controlling. Ultimately controlling the coalescence rate is only possible through knowledge of the material properties, and the use of a programmed and well-characterized time-temperature history of the growth environment [86].

Significant past efforts, of both experimental and theoretical nature, have been dedicated towards predicting primary particle sizes for nanoparticles grown from a vapor. These include the study of the sintering kinetics of Titania (TiO_2) nanoparticles in free jets and the use of a simple coalescence-collision time crossover model to determine the shapes of primary particles [87, 88]; TEM observations of TiO_2 primary particle sizes during sintering in heated gas flows [9]; or the analysis of growth characteristics of silica (SiO_2) [89–91] nanoparticles in aerosol reactor cells [92]. Models of nanoparticle coalescence in non-isothermal flames have been developed which employ population balance equations that are variants of the Smoluchowski equation [93]. Sectional models for aggregate aerosol dynamics accounting for gas-phase chemical reaction and sintering have also been developed to determine primary and aggregate particle size distributions under varying reactor temperatures [89].

It needs to be highlighted here that all of the afore-mentioned works on the prediction of primary particle sizes are primarily built on *the underlying assumption that particles were always at the background gas temperatures*. The only closest and earliest experimental work dealing with energy release during condensation of

aerosol clusters possibly carried out by Freund and Bauer [94] in their studies related to the homogeneous nucleation of metal vapors. Here, it will be critical to note that certainly on the experimental side, determination of particle temperature over extremely short time scales, as will be discussed in length in this section, would call for highly determined and involved experimental efforts to probe such effects.

Among some of the seminal works in relatively recent years, Lehtinen and Zachariah had shown [86, 95] that the exothermic nature of the coalescence process could significantly alter the sintering rate of nanoparticles. Moreover, they had demonstrated some unique results indicating that background gas pressures and volume loading of the material could significantly alter the overall temporal energy balance of coalescing particles, and could be used as effective process parameters to tailor primary particle sizes and the onset of aggregation [95]. The motivation for such novel observations stemmed from an earlier molecular dynamics (MD) study by Zachariah and Carrier [34] investigating the coalescence characteristics of silicon nanoparticles. This work had demonstrated a significant increase in nanoparticle temperature while undergoing coalescence. The formations of new chemical bonds between particles in the aftermath of collisions result in large heat release, and neck formations between the particles. This heat release may, under some conditions, result in an increase in particle temperature well above the background gas. Thus, the articles from Lehtinen and Zachariah [86, 95] had particularly reported that the particle coalescence is largely dominated by solid-state diffusion mechanism, which is an extremely sensitive function of temperature. Hence, the increase in particle temperature itself bears important effects on the coalescence dynamics. In fact, it was shown that for Si nanoparticle coalescence, in some cases, such effects could reduce the coalescence time by several orders of magnitude! *However, an important point of observation is that these studies did not consider ensemble aerosol effects, which led to the follow-up article by Mukherjee* et al. [44] *that developed a detailed KMC model to capture the ensemble effects of non-isothermal coagulation and coalescence on the growth dynamics of energetic nanoparticles. This will also constitute the main subject of this chapter*. Here, ensemble effects refer to random collision/coalescence processes between particle/aggregate pairs of any sizes and shapes, where simultaneous coalescence of all agglomerates that have undergone collisions at any instant of time are allowed to take place.

In light of the aforementioned observations, the following sub-sections in this chapter will largely focus on the work by Mukherjee et al. [44] that had developed a Monte Carlo based model in the lines of the earlier works of Efendiev and Zachariah [48] to extend their work on particle coagulation by incorporating non-isothermal finite rate coalescence processes. Through this work we will investigate here the inter-relationships of heat release and coalescence, as already proposed by Lehtinen and Zachariah [86, 95]. In doing so, we will present the details of a kinetic Monte Carlo (KMC) method developed and used by Mukherjee et al. [44] to study the effect of gas temperature, pressure and material volume loading on the heat release phenomenon during the time evolution of a nanoparticle cloud growing by random collision/coalescence processes. The significance of these

background process parameters in predicting the primary particle growth rates will also be discussed and analyzed. Largely, the role of non-isothermal coalescence process in controlling primary particle growth rates and aggregate formation for typical Si nanoparticles are discussed here. But, we will also present some significant highlights of findings from the titania (TiO_2) nanoparticle studies. The choice of these two materials is based on the large body of earlier works that have focused on them primarily due to the industrial importance of these particles, and their energetic behaviors.

3.1 Mathematical Model and Theory

3.1.1 Smoluchowski Equation and Collision Kernel Formulation

The particle size distribution of a poly-disperse aerosol undergoing coagulation can be described by the Smoluchowski equation as:

$$\frac{dN(t,V_j)}{dt} = \frac{1}{2}\int_0^{Vj} K(V_{i,}V_j - V_i)N(t,V_i)(t,V_j - V_i)dV_i - N(t,V_j)\int_0^{\infty} K(V_j,V_i)N(t,V_i)dV_i \tag{29}$$

where, t is the time, $K(V_i, V_j) = K_{i,j}$ is the kinetic coagulation kernel for the particles chosen with volume V_i and V_j and N (t, V_j) is the number density of the j-cluster [85].

The appropriate form of the coagulation or collision kernel depends on the Knudsen size regime of the growth. The kernel for the free molecule regime takes the form [85]:

$$K_{ij}^F = K^F(V_i,V_j) = \left(\frac{3}{4\pi}\right)^{\frac{1}{6}}\left(\frac{6k_BT_p}{\rho_p}\right)^{\frac{1}{2}}\left(\frac{1}{V_i}+\frac{1}{V_j}\right)^{\frac{1}{2}}\left(V_i^{1/3}+V_j^{1/3}\right)^2 \tag{30}$$

where, k_B denotes the Boltzmann constant, T_p is the particle temperature considered for collision, ρ_p is the particle density (assumed constant).

For the work presented in this section, one has to bear in mind that in free molecular regime the temperature dependence of collision kernel ($K_{ij}^F \propto T_p^{1/2}$) arises from the mean thermal speed of the nano particles derived from kinetic theory and expressed in the form: $\bar{c}_i = \left(8k_BT_p/\pi_\rho pV_i\right)^{1/2}$. Although the kernel has a weak dependence on the temperature, in this case the particle temperatures can become significantly higher than the background gas temperature. While formulating the

collision kernel, the present model considers its dependence on the particle temperature during the coalescence process. Hence, the above collision kernel takes the form:

$$K_{ij}^{F} = K^{F}(V_i, V_j) = \left(\frac{3}{4\pi}\right)^{\frac{1}{6}} \left(\frac{6k_B}{\rho_p}\right)^{\frac{1}{2}} \left(\frac{T_i}{V_i} + \frac{T_j}{V_j}\right)^{\frac{1}{2}} \left(V_i^{1/3} + V_j^{1/3}\right)^2 \tag{31}$$

where, T_i and T_j are the respective particle temperatures in the system considered for collision.

3.1.2 Energy Equations for Coalescence Process

During coalescence, a neck rapidly forms between the particles, which transforms into a spherule, and slowly approaches a sphere coupled with which is the particle temperature rise due to heat release as demonstrated by Zachariah and Carrier [39] and indicated by the schematic in Fig. 8.

Let us consider the case where, based on the collision probabilities, a typical collision event has successfully occurred between two spherical particles of sizes, V_i and V_j. Then upon coagulation it forms a new particle of volume $V_i + V_j$. It consists of N atoms or units which would essentially undergo the coalescence process and hence, would be used for formulating the typical energy equations and the corresponding heat release associated with modeling the entire process for all such particles. We assume that the energy E of a particle throughout the coalescence process can be described with bulk and surface contribution terms [96]:

$$E = \underbrace{N_W\left[\varepsilon b(0) + c_V T_p\right]}_{E_{bulk}} + \underbrace{\sigma_s a_p}_{E_{surf}} \tag{32}$$

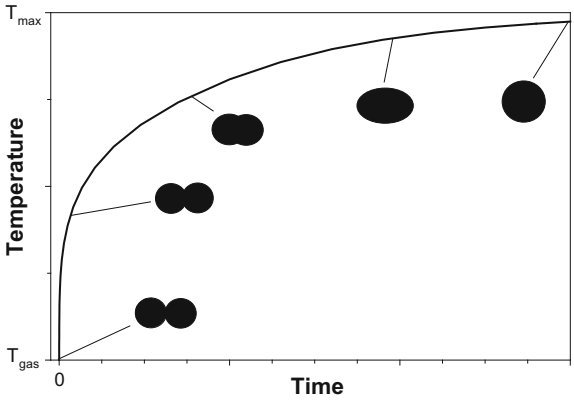

Fig. 8 Schematic representation of the temporal evolution of particle temperature and shape during nanoparticle coalescence

where, a_p is surface area of the coalescing particle pair, σ_s the surface tension, ε_b (0) the bulk binding energy (negative) at zero temperature, c_v the constant volume heat capacity (mass specific, J/kg-K) and N_w is the equivalent mass (kg) of N atoms in the particle pair undergoing coalescence. Under adiabatic conditions considered over a particle pair, the energy E would be constant, while the coalescence event will result in a decrease in the surface area, a_p and therefore an increase in particle temperature.

Any change in total energy, E of the particle (or, aggregate) can only result from energy loss to the surroundings, by convection, conduction to the surrounding gas, radiation, or, evaporation. Thus, for the temporal energy conservation equation for a particle (or, aggregate) we may write:

$$\frac{dE}{dt} = N_w c_v \frac{dT_p}{dt} + \sigma_s \frac{da_p}{dt} = -Z_c m_g c_g \left(T_p - T_g\right) - \varepsilon \sigma_{SB} a_p \left(T_p^4 - T_g^4\right) - \frac{\Delta H_{vap}}{N_{av}} Z_{ev} \tag{33}$$

where, T_p is the particle temperature, T_g is the gas temperature (K); c_g the mass specific heat capacity and m_g is the mass of gas molecules (kg). The emissivity of particles is ε, σ_{SB} is the Stefan-Boltzmann constant, ΔH_{vap} is the enthalpy of vaporization (J/mole) and N_{av} is the Avogadro number. Z_c is collision rate (s^{-1}) of gas-particle interactions in the free-molecule range and Z_{ev} is evaporation rate of surface atoms based on calculation of heterogeneous condensation rate (s^{-1}) of atoms on the particle surface.

The second term on the left hand side of Eq. 33 is the heat release due to coalescence arising from surface area reduction. The first and second terms on the right hand side of the equation are heat losses due to collisions with gas molecules, and radiation respectively, while the last term represents the heat loss due to evaporation from the particle surface.

The surface area reduction term in Eq. 33 is evaluated with the help of the well-known linear rate law [97] for final stages of coalescence:

$$\frac{da_p}{dt} = -\frac{1}{\tau_f}\left(a_p - a_{sph}\right) \tag{34}$$

where the driving force for area reduction is the area difference between the area of coalescing particles, a_p and that of an equivalent volume sphere, a_{sph}. Equation 34 has been widely used to model the entire process from spherical particles in contact to complete coalescence, since the overall sintering stage is rate controlled by the initial growth to a spheroid [97].

With the substitution, the non-linear differential equation for particle temperature can be expressed as:

$$N_w c_v \frac{dT_p}{dt} = \frac{\sigma_s}{\tau f}\left(a_p - a_{sph}\right) - Z_c m_g c_g \left(T_p - T_g\right) - \varepsilon \sigma_{SB} a_p \left(T_p^4 - T_g^4\right) - \frac{\Delta H_{vap}}{N_{av}} Z_{ev} \tag{35}$$

where, τ_f is characteristic coalescence, or fusion time defined as:

$$\tau_f = \frac{3 k_B T_p N}{64 \pi \sigma_s D_{eff}} \text{ where, } D_{eff} = D_{GB}\left(\frac{\delta}{d_{p\,(small)}}\right) \tag{36}$$

D_{eff} being the atomic diffusion coefficient that brings in significant non-linearity in the above equation as discussed in details later in this section. The above formulation for D_{eff} is derived based on the earlier works of Wu et al. [98]. D_{GB} is the solid-state grain boundary diffusion coefficient having the Arrhenius form: $D_{GB} = A \exp\left(-B/T_p\right)$, where σ_s is the particle surface tension, δ the grain boundary width (Table 1) and $d_{p(small)}$ is the diameter of the smallest particle in the coalescing cluster undergoing grain boundary diffusion process. The logic assumed here is that the smaller particle in any aggregate would coalesce faster into the larger ones, thereby determining the characteristic coalescence time. The values for pre- exponential factor A and activation energy term B are presented in Table 1.

Z_c, the gas–particle collision rate (s^{-1}) in the free-molecule regime results in conduction heat loss from the particle to the surrounding gas and is obtained from kinetic theory as:

$$Z_c = \frac{p_g a_p}{\sqrt{2\pi m_g k_B T_g}} \tag{37}$$

where a_p is the area of the coalescing particle pair and hence, varying in time according to the rate law (Eq. 34) and p_g is the background gas pressure.

Z_{ev}, the evaporation rate of surface atoms (s^{-1}) is determined by detailed balancing [99], and evaluated from the kinetic theory based calculation of the heterogeneous condensation rate on particle surface of area at the saturation vapor pressure given as [85]:

$$Z_{ev} = \frac{\alpha_c p_d a_p}{\sqrt{2\pi m k_B T_p}} \tag{38}$$

where, α_c is the accommodation coefficient assumed to be unity, p_d is the saturation vapor pressure over the droplet (spherical particle) and determined from the Kelvin effect.

Thus, for the evaporative heat loss term:

$$\frac{\Delta H_{vap}}{N_{av}} Z_{ev} = \frac{\Delta H_{vap}}{N_{av}} \left(\frac{\alpha_c a_p p_s}{\sqrt{2\pi m k_B T_p}}\right) \exp\left(\frac{4\sigma_s v_m}{d_p R T_p}\right) \tag{39}$$

Table 1 Thermodynamic, and diffusional properties for Silicon and Titania[a]

Properties	Silicon	Titania	Reference
Bulk melting point, T_m (K)	1683	2103	[151]
Density, ρ_p (kg/m^3)	2330	3840	[151, 160]
Solid surface tension, σ_s (J/m^2)	0.9	0.6	[88, 151]
Liquid surface tension, σ_l (J/m^2)	–	0.34	[93, 95]
Constant volume heat capacity, c_v(J/kg-K)	729	800	[151]
Heat of vaporization, ΔH_{vap} (J/mole)	384,000	598,712	[151, 157]
Heat of fusion, L (J/mole)	–	47,927	[95]
Diffusion coefficient parameters			
Pre-exponential factor, A (m^2/s)	4.69×10^{-7}	7.2×10^{-6}	[39, 161]
Activation energy, E_{ac} (kJ/mole)	62.84	286	[39, 161]
Normalised activation energy, B = (E_{ao} / 8.31) (K)	7562	34,416	
Saturation vapor pressure relations			
(a) Silicon			[100]
$\log_{10} p_s = a + \frac{b}{T_p} + c \log_{10} T_p + dT_p + eT_p^2$ (p_s in mm of Hg; T_p in K)			
$a = 315.0687$; $b = -7.1384 \times 10^4$; $c = -89.68$; $d = 8.3445 \times 10^{-3}$ and $e = -2.5806 \times 10^{-9}$			
(b) Titania			
$\log_{10} p_s = a + \frac{b}{T_p} + cT_p$ (p_s in Pa or, N/m^2; T_p in K)			[157]
$a = 16.20$; $b = -30361$ and $c = -0.492 \times 10^{-3}$			

[a]Reprinted from *J. Chem. Phys.* ***119****, 3391 (2003)* [44], with the permission of AIP Publishing

where, p_s is the saturation vapor pressure (Pa) over flat surface at the instantaneous particle temperature during coalescence [100] and v_m is the molar volume (m^3/mole). The equations for vapor pressure of Si and TiO_2 used in the present work have been given in Table 1. The exponential dependence on particle temperature implies that as the particles heat by coalescence, significant evaporative cooling might take place.

As discussed earlier, the coalescence process reduces the surface area according to the rate law equation given in Eq. 34, which result in surface energy loss. In an adiabatic case all this energy would be partitioned into the internal thermal energy of particles. However, losses to the surroundings will have a significant impact on the particle temperature and therefore its coalescence dynamics. A detailed

description of the coalescence dynamics and energy transfer is obtained by numerically solving the coupled Eqs. (34) and (35).

It is to be noted that Eq. 33 is highly non-linear in temperature through the exponential dependence of the solid-state atomic diffusion coefficient D_{GB} in the particle, which is expressed, as:

$$D_{GB} = A \exp\left(-\frac{B}{T_p}\right) \tag{40}$$

where, A and B are material dependent constants (Table 1). Thus, in typical solid-state sintering, if particle temperature increases due to heat release effects, then lower gas pressures, higher volume loadings (higher collision frequency) and high gas temperatures may result in particle heat generation being larger than heat loss to the surroundings. This, in turn, increases diffusion coefficient (D_{eff}), reduces characteristic coalescence time, τ_f and hence, further serves to increase the particle temperature.

A further complication that may occur during a coalescence event, is that before the resulting particle can relax back to the background gas temperature, it may encounter yet another collision. This would be the case when the characteristic coalescence time is larger than the collision time $(\tau_f > \tau_{coll})$, thereby generating aggregates. On the other hand, if $\tau_f < \tau_{coll}$, particles have sufficient time to coalescence and no aggregate is formed. Therefore, the formation of the often-observed aggregate structure is determined by the relative rates of collision and coalescence. However, the heat release from coalescence, if not removed efficiently from the particle, will keep the coalescence time small relative to the collision time and delay the onset of aggregate formation. Our goal is to understand the non-linear dynamics leading to the formation of aggregates and its effect in terms of growth characteristics of primary particles that go on to form these aggregates.

3.1.3 Effect of Lowered Melting Point of Nanoparticles on Coalescence

The diffusion mechanism in nano-sized particles might differ from bulk diffusion processes and has been previously studied [39]. Although, the phenomenon is not clearly understood, for most practical purposes of this work, one might assume that classical concepts of volume, grain boundary, and surface diffusion are applicable [98]. Grain boundary diffusion has been pointed out as the most significant solid-state diffusion process in polycrystalline nano-sized particles [39, 98], though the exact processes for atomic diffusion depend on the crystalline structures of particles.

The diffusion coefficient being very sensitive to the phase (molten or solid), care must be taken to track the phase changes during the growth process. Of particular importance, in the size range of interest, is the size dependence of the melting point

of ultrafine particles. The empirical relation approximating the melting point of nano particles is given as [101]:

$$T_{mp}(dp) = T_m\left[1 - \frac{4}{L\rho_p d_p}\left(\sigma_s - \sigma_1\left(\frac{\rho_p}{\rho_1}^{2/3}\right)\right)\right] \tag{41}$$

Here, T_m is the bulk melting point, L the latent heat of melting (J/kg), σ_s and σ_l are the surface tensions (J/m^2), and ρ_p and ρ_l are the respective solid and liquid phase densities (kg/m^3). The various material property values are presented in Table 1.

This effect of lowered melting point on particle coalescence process turns out to be of particular significance the case of titania growth studies, since these investigations are typically conducted in the 1600–2000 K range. Application of Eq. 41 would show that for titania that has a bulk melting point of 2103 K, the melting point drops to about 1913 K at 5 nm and 1100 K for a 1 nm particle. In such a scenario, at typical flame temperatures encountered in experiments, particles may coalesce under a viscous flow mechanism as opposed to a solid-state diffusion mechanism. It also implies that particles may encounter a phase transition during a coalescence event simply due to the energy release process, i.e., $T_p(t) > T_{mp}(d_p)$.

To take this into account, the diffusion process and corresponding characteristic coalescence times for the TiO_2 cases meed to be computed as follows: (1) when $T_p(t) < T_{mp}(d_p)$, a solid state grain boundary diffusion process was assumed to calculate coalescence time as given by Eq. 40 and (2) when $T_p(t) > T_{mp}(d_p)$, a viscous flow mechanism was used [102] as:

$$\tau_f = \frac{\mu d_{eff}}{2\sigma_l} \tag{42}$$

where, μ is the viscosity at the particle temperature; σ_l is the liquid surface tension of particle and d_{eff} was taken to be proportional to the instantaneous effective particle diameter (V_p/a_p), i.e., $d_{eff} = 6V_p/a_p$.

The viscosity, μ is estimated from empirical relations [103] as a function of particle temperature T_p, and melting point for the corresponding particle size, $T_{mp}(d_p)$. The empirical relation for size dependent viscosity of nanoparticles is given as:

$$\mu = 10.87 \times 10^{-7} \frac{\left[M.T_{mp}(d_p)\right]^{1/2} \exp\left(\frac{L}{RT_p}\right)}{v_m \exp\left[\frac{L}{RT_{mp(d_p)}}\right]} \tag{42a}$$

where, L is the latent heat of fusion (J/mole), R is the universal gas constant (J/mole-K), v_m is the molar volume (m^3/mole) and M is the molar weight (kg/mole).

3.1.4 Radiation Heat Loss Term for Nanoparticles: A Discussion

Thermal radiation from small particles is a subject of considerable interest and complexity and has been discussed by a number of earlier works [104–107]. The prime concern for this work is in the emissivity values needed in Eq. 35 to determine the effect of radiation heat loss in typical nanoparticles. However unlike bulk materials, for particles smaller than the wavelength of thermal radiation, the emissivity becomes a strong function of the characteristic dimension of the particle [108]. It is well known from Rayleigh scattering theory that the absorption efficiency: $Q_{abs} \propto X$, where, X is the non-dimensional particle size parameter given as: $X = \pi d_p/\lambda$, λ being the wavelength of emitted radiation considered. For very fine particles and for the wavelength range of 800 nm or greater (for thermal radiation), the values for absorption efficiency (Q_{abs}) are extremely small (around 10^{-5}–10^{-7}).

Now, from Kirchhoff's law for radiation from spherical particles: $Q_{abs} = \varepsilon$ [109]. Hence, we conclude that emissivity for thermal radiations from nanoparticles in the Rayleigh limit ($d_p \ll \lambda$) are negligible unless we operate at extremely high temperatures. Thus, for all practical purposes, the radiation heat loss term for the present study can be assumed to be negligible and dropped from Eq. 35 to give its final form as:

$$N_w c_v \frac{dT_p}{dt} = \frac{\sigma_s}{\tau_f}\left(a_p - a_{sph}\right) - Z_c m_g c_g \left(T_p - T_g\right) - \frac{\Delta H_{vap}}{N_{av}} Z_{ev} \tag{43}$$

3.2 *Modeling Non-isothermal Coagulation and Coalescence: Coagulation Driven KMC Model*

Monte Carlo (MC) methods have recently been shown to be a useful tool for simulating coagulation-coalescence phenomena. They have the advantage that both length and time scale phenomena can be simultaneously solved without a single unifying governing multi-variate equation. Furthermore, MC methods provide an intuitive tool in simulating the random coagulation process without any a priori assumption of the aerosol size distribution. To this end, Rosner and Yu [110] have used MC methods to demonstrate the "self-preserving" asymptotic pdf for bivariate populations in free molecular regime. Kruis et al. [47] have used MC methods to establish its suitability for simulating complex particle dynamics. These works have clearly demonstrated the statistical accuracy of MC method by comparing it with the theoretical solutions for aggregation and the asymptotic self-preserving particle-size distribution [85] for coagulation. In a parallel work, Efendiev and Zachariah [48] had also demonstrated the effectiveness of the method, by developing a hybrid MC method for simulating two-component aerosol coagulation and internal phase-segregation. Furthermore, it has been shown rigorously by Norris [111] that the MC approach approximates the aerosol coagulation equation for

number concentration of particles of any given size as a function of time. The kinetic Monte Carlo (KMC) model, presented here from Mukherjee et al. [44], has been primarily based on the earlier works of Liffman [46] Smith and Matsoukas [78] and the recently developed hybrid MC method of Efendiev and Zachariah [48].

Among a vast number of existing MC techniques developed for simulating the growth of dispersed systems, the two primary ones fall under the category of Constant-Number (*Constant-N*) and the Constant-Volume (*Constant-V*) methods. The classical *Constant-V* method samples a constant volume system of particles, and with the advancement of time reduces the number of particles in the sample due to coagulation. This is the same approach as any other time-driven numerical integration and hence it does not offer a uniform statistical accuracy in time. This reduction in the sample usually needs simulation for large number of initial particles to ensure an acceptable level of accuracy in the results. This might lead to an under-utilization of the computational resources [112]. This problem can be overcome by a *Constant-N* method by refilling the empty sites of the particle array in the system, with copies of the surviving particles. This method has been shown to be more efficient, and has been employed by Kostoglou and Konstandopoulos [112], Smith and Matsoukas [78] and Efendiev and Zachariah [48] for simulation of particle coagulation.

To overcome this loss of accuracy due to continuously decreasing particle number arising from coagulation a discrete refilling procedure, as proposed by Liffman [46], was used in which whenever the particle number dropped to a sufficiently small value (50% of the initial number) the system was replicated. The *Constant-N* approach can be implemented in two general ways. The first approach is to set a time interval, Δt and then use the MC algorithm to decide which and how many events will be realized in the specified time interval [46, 113]. This essentially amounts to integrating the population balance forward in time and requires discretization of the time step. In the second approach, a single event is chosen to occur and the time is advanced by an appropriate amount to simulate the phenomenon associated with the event [45, 114]. This approach does not require explicit time discretization, and has the advantage that the time step, being calculated during the simulation, adjusts itself to the rates of the various processes.

The work presented in this section employs the second approach for describing particle coagulation, while the first approach is used for simulating particle coalescence, once a coagulation event has been identified. Thus, more precisely, first a single coagulation event is identified to occur for the particles in the system and then, the mean inter-event time required, ΔT for the next coagulation event to occur is computed. Then, during this time interval, the coalescence process is simulated along with the associated energy release for all the particles in our system. It is worth mentioning for clarity that at any identified inter-event time between two successive particle (or, aggregates) collisions, there will be coalescence taking place for other system particles that had collided earlier in time.

It is important to recognize that the mean characteristic collision time ($\tau_{coll} \approx \tau_c$) essentially signifies the mean time interval that any particular particle (or, aggregate) has to wait before it encounters another collision, while the mean inter-event

time represents the time between any two successive collision events (ΔT) amongst any two particles (or, aggregates) in the system. The latter, also becomes the MC simulation time-step for the current model.

3.2.1 Implementation of MC Algorithm: Determination of Characteristic Time Scales for Coagulation

The MC algorithm presented here is developed based on Mukherjee et al.'s work [44] wherein a simulation system with initial particle concentration of C_0 is considered. A choice of the number of particles N_0 that can be efficiently handled in the simulation, defines the effective computational volume: $V_0 = N_0/C_0$. To connect the simulations to real time, the inter-event time between any two successive collisions or the MC time step, ΔT_k is inversely proportional to sum of the rates of all possible events:

$$\Delta T_k = \frac{V_0}{\sum_l R_l} = \frac{2N_0}{C_0 \sum_{i=1}^{N_{k-1}} \sum_{i=1}^{N_{k-1}} K_{ij}^F} \tag{44}$$

where, $R_l = K_{ij}$ is the rate of event l, defined as the coagulation of the pair (i, j), K_{ij} is the coagulation kernel for sizes i and j, and $V_0 = N_0/C_0$ is the actual volume represented in the simulation system for particle concentration, C_0 and number of simulation particles, N_0. For computational time efficiency, a mean coagulation probability, $\left\langle K_{ij}^F \right\rangle$ is defined as:

$$\left\langle K_{ij}^F \right\rangle = \frac{\sum_{i=1}^{N_{k-1}} \sum_{j=1}^{N_{k-1}} K_{ij}^F}{N_{k-1}(N_{k-1} - 1)} \tag{45}$$

Hence, the final form for the Monte Carlo time step can be given as:

$$\Delta T_k = \frac{2N_0}{C_0 \left\langle K_{ij}^F \right\rangle N_{k-1}(N_{k-1} - 1)} \tag{46}$$

Now, for each collision event, we use the inter-event time (ΔT_k or, simply ΔT) determined above, to simulate the coalescence process for *all particles* by integrating the surface area reduction and the energy equations. Then based on the mean values of the area, volume and temperature of the particles in the system calculated at the end of each MC time step, the mean characteristic collision time (τ_c) in the free molecular regime is estimated from the self-preserving size distribution theory of Friedlander [85] as:

$$\tau_c = 3/B \text{ where } B = (\alpha/2)\left(\frac{6k_B\overline{T}_p}{\rho_p}\right)^{1/2}\left(\frac{3}{4\pi}\right)^{1/6}\phi\overline{V}_p^{(-5/6)} \tag{47}$$

where, $\overline{T}_p$ and $\overline{V}_p$ stands for the mean particle temperature and volume, α, a dimensionless constant equal to 6.55 [115], ρ_p is the density of the particle material (assumed to be temperature independent) and ϕ is the material volume loading in the system considered.

Thus, for each inter-event time ΔT, an integration time step Δt for the coalescence process is defined as:

$$\Delta t = \frac{\Delta T}{n_{max}}, \quad \text{and} \quad n_{max}\frac{\Delta T}{\tau_f} \times p \tag{48a, b}$$

where, n_{max} is the number of iterative loops for the numerical integration in time; τ_f is the characteristic coalescence time previously defined in Eq. 42 and p is any integer value normally chosen as: $p = 10$. This method of choosing the numerical time step ensures sufficient discretization of time step to obtain desired resolution for simulating the coalescence process over the particular inter-event collision time and characteristic sintering time, both of which are sensitive to size and temperature.

In order to implement the numerical computation, the coagulation probability is defined as:

$$p_{ij} = \frac{K_{ij}^F}{K_{max}^F} \tag{49}$$

where, K_{max}^F is the maximum value of the coagulation kernel among all droplets. At each step two particles are randomly selected and a decision is made whether a coagulation event occurs based on p_{ij}. If the event takes place, then the inter event time, ΔT us calculated as shown earlier and the subsequent coalescence process is simulated. As indicated earlier by Smith and Matsoukas [78] as well as Efendiev and Zachariah [48], this probability should, in principle, be normalized by the sum of all K_{ij} but the choice of K_{max}^F is commonly employed in order to increase the acceptance rate while maintaining the relative magnitude of probabilities.

In the current implementation of the KMC model, a coagulation event occurs only if a random number drawn from a uniform distribution is smaller than the coagulation probability, $p_{ij.}$ If the coagulation is rejected, two new particles are picked and the above steps are repeated until a coagulation condition is met. Upon successful completion of this step the selected particles with volumes V_i and V_j are combined to form a new particle with volume $V_i + V_j$ and total number of particles in the system is decreased by unity.

When the number of particles due to this repeated coagulation process drops to half of the initial value, the particles in the system are replicated. In order to

preserve the physical connection to time, the topping up process must preserve the average behavior of the system like the volume loading or the particle number density corresponding to the time prior to the topping up. In such time-driven MC processes, one ensures that the inter-event time for particle collisions stays the same by increasing the effective simulation volume, V_0 in proportion to the increase in particle number in the topped up system.

In relating the MC simulation to the real physics of the coalescence process, the schematic indicating the role of different time scales of events is helpful and is shown in Fig. 9. This figure, shows the relative magnitudes of the three time scales: the characteristic cooling time (τ_{cool}), characteristic collision time (τ_c) and characteristic coalescence or fusion time (τ_f) that are critical in determining whether a particle colliding would undergo complete sintering, release more heat and grow into a larger uniform primary particle or, would quickly quench and lose heat to form aggregates with larger surface area, but smaller primary particle sizes. If a criteria is met where by $\tau_{cool} > \tau_c > \tau_f$, one should expect to see fully sintered primary particles with large heat release. Whereas, if $\tau_c < \tau_f$, then the particles cannot fully sinter before they encounter the next collision, and this gives rise to the formation of aggregates.

3.2.2 Model Metrics and Validation for the KMC Algorithm

The number of MC particles required to achieve statistical accuracy in the system under study were determined from analyses of the characteristic collision and fusion times, temperature rise and other properties for two systems consisting of 1000 and 10,000 particles. Although computation time increases significantly, there is insignificant change in the mean results for characteristic collision times, fusion times and particle temperature of these two systems indicating the attainment of statistical equilibrium. Thus, all results presented in the following section on results from the current KMC simulation have been obtained by using systems of 1000

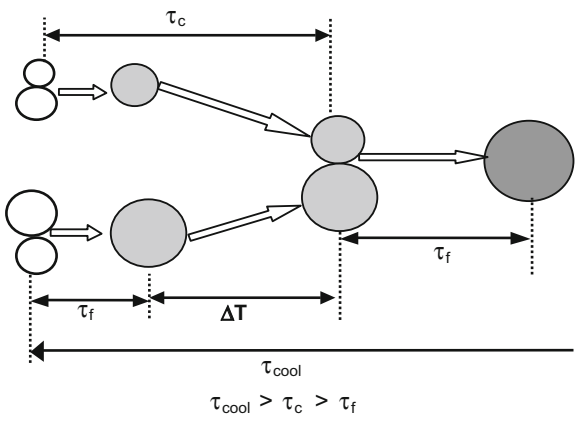

Fig. 9 Schematic diagram indicating the various time scales; mean inter-event time (ΔT), characteristic coalescence/fusion (τ_f), characteristic collision (τ_c) and the mean cooling time for particles (τ_{cool})

particles. It may be recalled here that the use of topping up technique, as proposed by Liffman [46], also reduces the statistical errors in the simulations even with a smaller number of particles, while requiring lesser computer memory. For all the studies presented here, the average simulation time for a 1000 particles system with a volume loading of 10^{-4} was anywhere between 15 and 2 h (depending on the parameters of the case study) while running on IBM–SP machines at the Minnesota Supercomputing Institute with eight 1.3 GHz power4 processors sharing 16 GB of memory.

For ease of scaling, the simulations presented in the following sections starts with the assumption of a monodisperse system of 1 nm diameter particles. Also, it was observed that the increase in background gas temperature due to heat release from coalescence is insignificant and hence, gas temperature was assumed to be constant throughout in all the simulation results discussed here. The representative results presented here for the discussions are for silicon and titania nanoparticles. The thermodynamic properties of Si and TiO_2, including density, heat capacity, latent heat of fusion/melting and surface tension are assumed to be particle size independent [91, 96], and are reported in Table 1.

The MC algorithm presented here was validated for the coagulation study, the details for which can be found in Mukherjee et al. [44], and its accuracy was found to be in excellent agreement with sectional model simulations of Lehtinen and Zachariah [34]. As the model metrics, we present here, as seen in Fig. 10, the particle size distributions at long times, which when compared with the numerical results of Vemury et al. [116], showed very good agreement with the known self-preserving size distribution seen for coagulating aerosols.

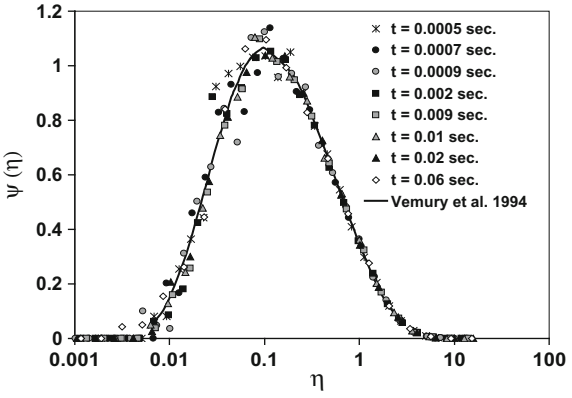

Fig. 10 Self-preserving size distribution for coagulation from Monte Carlo method compared with numerical results of Vemury et al. [43] and plotted as dimensionless number density, $\psi(\eta) = N\left(t,V_p\right)\overline{V}_p/N_\infty$ versus dimensionless volume, $\eta = V_p/\overline{V}_p$. Silicon at T_g = 320 K was considered assuming free molecular regime collision kernel

3.3 Results and Discussions: Effects of Process Parameters on Nanoparticle Growth via Coagulations and Non-isothermal Coalescence

3.3.1 Effect of Background Gas Temperature

The competing effects of heat release and bath gas cooling were assessed with simulations for Si nanoparticle growth carried out at gas temperatures of 325, 500 and 800 K with background gas pressure, $P_g = 100$ Pa and material volume loading, $\phi = 10^{-6}$. Shown in Fig. 11 are plots adopted from the results of Mukherjee et al. [44] that indicate the characteristic collision and coalescence times as a function of growth time. Such a plot has been proposed by Windeler et al. [87] to assess the competition between these two times and their crossing point. In Fig. 11a, the heavy dotted line represents the characteristic collision time, which is relatively independent of temperature and increases in time for a coagulation process because of the net decrease in particle number concentration. The coalescence time is a function of particle size and temperature as discussed before. For the work considered here, the coalescence energy release and the losses to the surrounding can significantly alter this time. The crossing point, as suggested by Windeler et al. [87], defines the onset of aggregation and enables primary particle size prediction. However we show later that the use of the crossing point between τ_f and τ_c to predict primary particle sizes might not be universally applicable. For the various gas temperatures studies presented here, we found that with increasing residence time, τ_f initially decreases, reaches a minimum, and then monotonically increases.

The decrease in the characteristic coalescence (fusion) time τ_f is actually associated with an increase in the particle temperature and is shown in Fig. 11b. Here we see that the particle temperature takes an abrupt and very rapid rise to a value well in excess of 1200 K. This is an indication that the characteristic cooling time under these conditions is slow relative to the fusion time, τ_f implying larger heat generation. Higher background temperatures show an earlier onset of elevated temperatures and a prolonged dwell time at higher temperatures due to the lower driving force for cooling. At the same time, delayed onset of heat release effects, generate larger aggregates trying to coalesce fully, which cause a stronger driving force for the heat generation arising from the surface area reduction term and hence, an increase in the net rise in particle temperature. Referring back to Fig. 11a, we see the minimum in the coalescence time roughly corresponds to the peak particle temperature achieved. Also, with increasing gas temperatures, for the same particle size distribution, the relative values of τ_f decrease but τ_c remains relatively unchanged. In the context of the current discussions on the comparison of characteristic times, we see from Fig. 11a, b that after the initial drop the coalescence time eventually rises, coupled with heat loss from particles, till it crosses the collision time curve. At this point one can reasonably conclude that aggregate formation has been triggered. Beyond this, in the region where $\tau_f > \tau_c$, the particles do not get sufficient time to fully sinter before the next collision takes place thereby

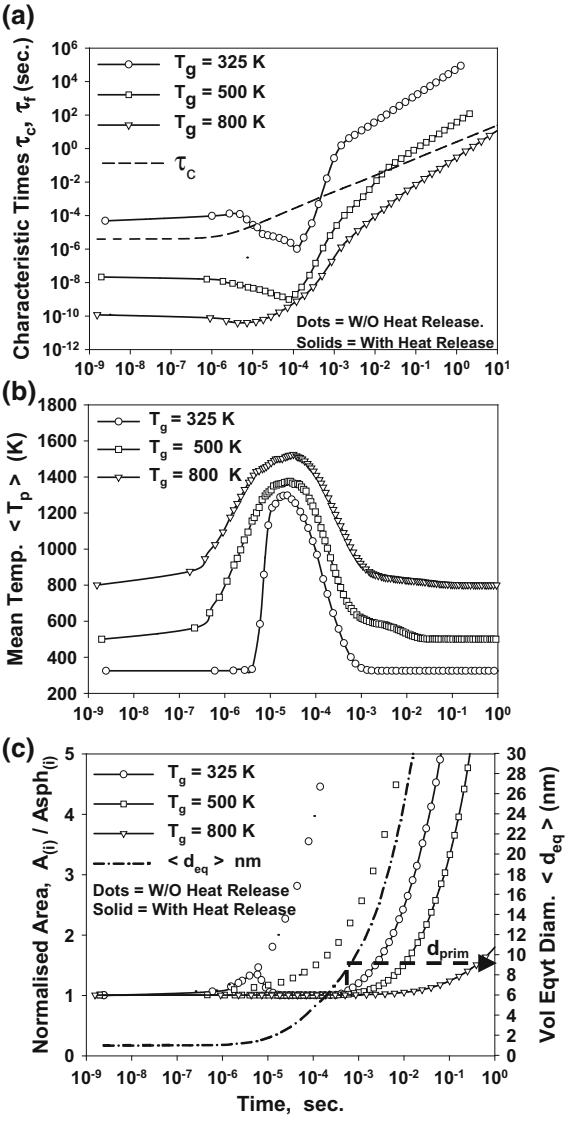

Fig. 11 Variations of **a** characteristic fusion (τ_f) and collision (τ_c) times, **b** mean particle temperature ($<T_p>$), and **c** normalized area (*left axis*) and mean volume equivalent diameters (*right axis*) with residence times for various background gas temperatures for Silicon; (P_g = 100 Pa and $\phi = 10^{-6}$). *Here, $A_{(i)}$: Particle area and $A_{sph(i)}$: Equivalent spherical area of corresponding particle*

forming aggregates. Eventually, the particles get sufficiently larger so that their heat capacity is large enough as to negate any significant temperature rise associated with coalescence and the growing particles return to the background temperature.

Higher background temperatures show an earlier onset of elevated temperatures and a prolonged dwell time at higher temperatures due to the lower driving force for cooling. At the same time, delayed onset of heat release effects, generate larger aggregates trying to coalesce fully, which cause a stronger driving force for the heat generation arising from the surface area reduction term and hence, an increase in the

net rise in particle temperature. Referring back to Fig. 11a, we see the minimum in the coalescence time roughly corresponds to the peak particle temperature achieved. Also, with increasing gas temperatures, for the same particle size distribution, the relative values of τ_f decrease but τ_c remains relatively unchanged. In the context of the current discussions on the comparison of characteristic times, we see from Fig. 11a, b that after the initial drop the coalescence time eventually rises, coupled with heat loss from particles, till it crosses the collision time curve. At this point one can reasonably conclude that aggregate formation has been triggered. Beyond this, in the region where $\tau_f > \tau_c$, the particles do not get sufficient time to fully sinter before the next collision takes place thereby forming aggregates. Eventually, the particles get sufficiently larger so that their heat capacity is large enough as to negate any significant temperature rise associated with coalescence and the growing particles return to the background temperature.

It is possible that with higher temperatures as $d\tau_f/dt$ approaches $d\tau_c/dt$ (at the crossing point, i.e., $\tau_f \approx \tau_c$), oblong particles with long necks and strong bonds are formed that would eventually go on to form aggregates. However, at lower temperature the crossing occurs within the heat generation regime and $d\tau_f/dt \gg d\tau_c/dt$ (at $\tau_f \approx \tau_c$). Thus, in this case, uniform spherical particles held together by weak Van der Waals' forces in the agglomerates are formed. This theory was also found to be consistent with the earlier work of Windeler et al. [87].

3.3.2 Effect of Background Gas Pressure

The conventional wisdom has held that background gas pressure has no role in the heat transfer during collision/coalescence process. This presumption has held sway because until very recently prior work had neglected the exothermic nature of coalescence. Lehtinen and Zachariah [86, 95] were the first to recognize this effect and conclude that gas pressure P_g, should have an impact on primary particle size.

The effect of P_g on τ_f at constant gas temperature for silicon (T_g = 500 K, $\phi = 10^{-6}$) is shown in Fig. 12a. Corresponding mean particle temperatures are shown in Fig. 12b. At 101 kPa the effect of heat release is negligible as the heat losses to the surroundings are evidently sufficiently facile. As one decreases the pressure however, the lowered heat loss term through conduction enables the particles to experience elevated temperatures. In these cases the lower the pressure the higher the particle temperatures. This self-heating is also reflected in the lowering of the characteristic sintering time seen in Fig. 12a. At the highest pressure simulated the role of heat release is unimportant, while with decreasing pressure we see a monotonic increase in primary particle size from roughly about 3 nm at 101 kPa to 13 nm 100 Pa. This increase clearly establishes the effect of gas pressure on the primary particle growth rates and as seen from Fig. 12b, reflects the higher particle temperatures experienced at lower pressures resulting from a lower heat loss rate by conduction. It is clearly noticed that the fusion and collision times presented in Fig. 12a show a crossing point independent of pressure! This result indicates that the crossing point may not be the best criteria for assessing the

spherical primary particle size, especially beyond the heat generation regime where the relative gradients of the characteristic times, i.e., $d\tau_f/dt$ and $d\tau_c/dt$ at the crossing point are close to each. The two gray points in Fig. 12a mark a noticeable change in $d\tau_f/dt$ indicating the time where the normalized surface area deviates from unity ($A/A_{sph} > 1$), and was used for determining the spherical primary particle sizes. Beyond this point, and before the particles are agglomerated (i.e., the

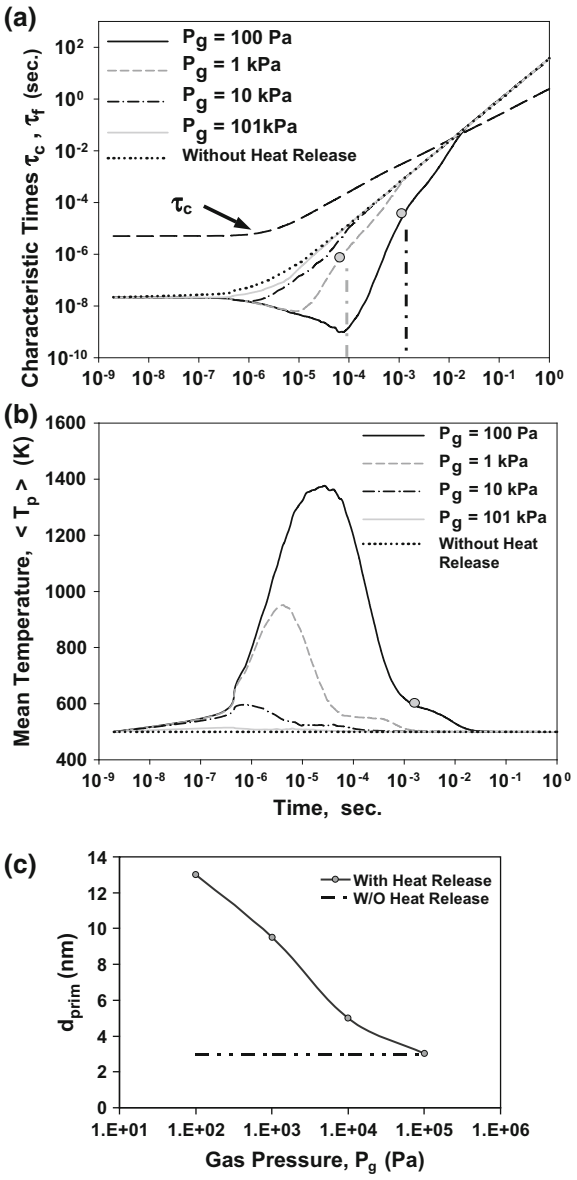

Fig. 12 Variations of **a** characteristic coalescence/fusion (τ_f) and collision (τ_c) times, and **b** mean particle temperature ($<T_p>$) with residence time along with heat release effects on primary particle sizes (d_{prim}) for various background gas pressures, P_g. (T_g = 500 K and $\phi = 10^{-6}$). *Grey point marks gradient change when* $A_{(i)}/A_{sph(i)} \geq 1$; *Results are for Si*

crossing point between τ_f and τ_c) the primary particles are non-spherical (possibly oblong with large necks) mainly due to the slow crossing point of τ_f and τ_c, as discussed in details earlier [87]. Thus, we estimate the primary particle size (d_{prim}) from the normalized area term ($A/A_{sph} > 1$) and the corresponding volume equivalent diameter as discussed earlier (not shown here) at the point of agglomeration. These results are presented in Fig. 12c.

The aforementioned model was also applied to TiO_2 nanoparticle growth under different gas pressures (P_g = 100 Pa, 1, 10 and 101 kPa) at T_g = 1600 K. The choice for the operating temperature was based on the process parameters used in the industry for TiO_2 production. It needs to be highlighted here that the present simulations trace the coagulation/coalescence of particles from the time precursor reactions leading to 100% conversion of precursors ($TiCl_4$ or, TTIP) to TiO_2 nanoparticles have been achieved, so that we have a sufficiently large particle number concentration and growth rates are purely due to collision/coalescence process without any nucleation effects.

We would like mention that the focus of the current chapter being energetic metal nanoparticles, we would briefly touch upon the significant results from the TiO_2 nanoparticle case studies. For further details on the TiO_2 case studies, the readers should refer to article by Mukherjee et al. [44]. The most significant aspect of the studies on the TiO_2 nanoparticle systems was that the results are able to capture the role of phase transition on growth along with the effect of size dependent melting point of nanoparticles. We rely on Eq. 41 to determine, for a given particle, if we are above or below the melting point at any instant in the coalescence process and use the appropriate sintering model (solid-state or viscous flow). This becomes essential since viscous flow characteristic times are 2–3 orders of magnitude lower than that for solid-state diffusion.

The heat release, and the rise in particle temperature in time due to the competing characteristic times of τ_f and τ_c are evident form Fig. 13a. Here, it needs to be pointed out that initially for small particle sizes (1 nm), $T_p(t) > T_{mp}(d_p)$ (from Eq. 41), particles are in molten state and hence, the characteristic coalescence time (τ_f) is very small so that particles coalesce almost instantly on contact and undergo rapid evaporative cooling. But as particle sizes increase due to coagulation/coalescence, corresponding melting points also increase and rise above the particle temperature, i.e., $T_p(t) < T_{mp}(d_p)$ and the particles shift over to the much slower solid-state diffusion mechanism followed by slow conductive losses only. These processes are clearly observed from the gradient changes in the τ_f and T_p during the particle energy relaxation periods in Fig. 13a, b. In line with our earlier discussions from the Si nanoparticle case studies, the size for the spherical primary particles at the cross-over point for τ_f and τ_c (see Fig. 13a) were determined from the criteria of $d\tau_f/dt \gg d\tau_c/dt$ for all the pressure case studies of 100 Pa–101 kPa. Furthermore, from Fig. 13b, it can be seen that the peak rise in particle temperature (i.e., in the region of viscous diffusion mechanism) does show significant variations for the different gas pressures. However, when the particle temperature relaxers (i.e., in solid-state diffusion region), the particle temperatures are higher for the P_g = 100 Pa case due to lesser heat loss resulting in a prolonged

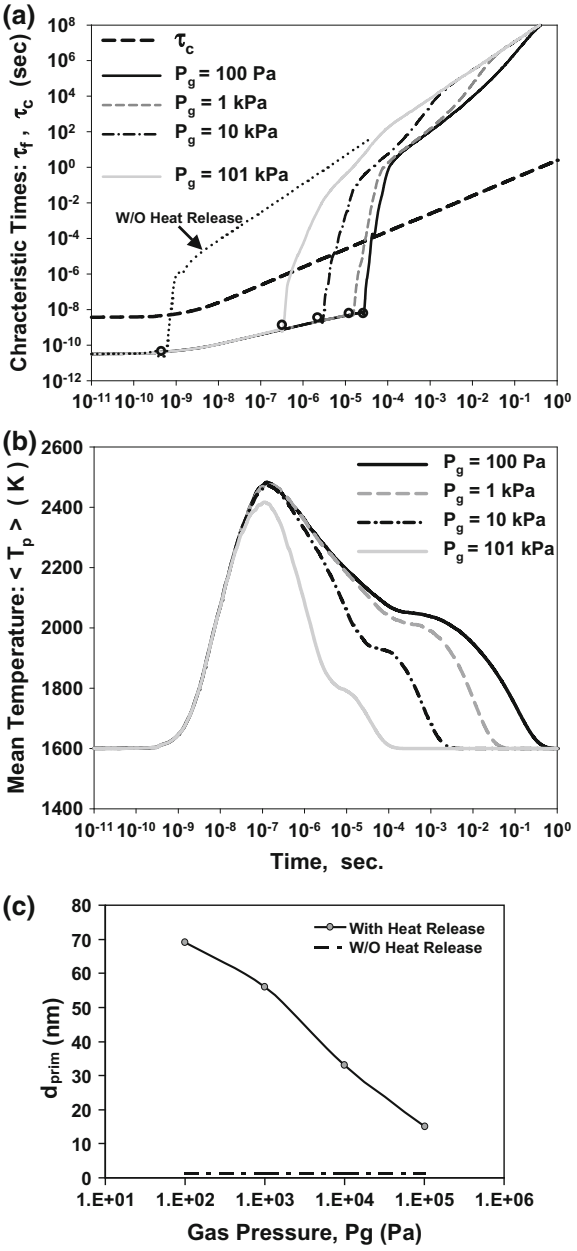

Fig. 13 Variations of **a** characteristic fusion (τ_f) and collision (τ_c) times, and **b** mean particle temperature ($<T_p>$) with residence times for various background gas pressures, P_g, *Open circle* indicates abrupt change in gradient corresponding to phase change from molten to solid-state; **c** Heat release effects on primary particle sizes (d_{prim}) for the aforesaid case. (T_g = 1600 K and $\phi = 10^{-3}$). *Results are for TiO_2*

and enhanced sintering mechanism over the time that competes with the heat loss terms in the energy balance. Finally, they cool down to background gas temperature indicated by the merging of all the fusion time gradients where τ_f keeps on increasing purely due to aggregate growth. Figure 13c illustrates the spherical

primary particle sizes as function of different gas pressures and shows the use of background pressure to alter primary particle size.

3.3.3 Effect of Volume Loading

Volume loading is another important process parameter that typically is not considered for detailed analysis in many studies of primary particle size predictions for nanoparticle coalescence processes. Common laboratory experiments are usually limited to low volume fractions ($\phi = 10^{-6}$) for ease of experimentation, particularly for those who use in situ optical probes. Industrial practice of course seeks to maximize production rate and typically operates at much higher volume fractions ($\phi = 10^{-3}$). Without the consideration of the exothermic nature of coalescence, it is natural to expect no role for the volume fraction. On the other hand, with heat release considered we might expect that under rapid coalescence conditions, where heat release is faster than energy loss to the surroundings, a higher collision rate might magnify the effect.

The model has been applied to various laboratory and industrial volume loadings in the range of $\phi = 10^{-6}$–10^{-3} for Si (Fig. 14). Here the Si example is most reflective of what might occur in typical low-pressure plasma synthesis of metal nanopartciels. In Fig. 14a, it is seen that all volume loadings considered result in elevated particle temperatures, however increased volume fraction results in higher temperatures for prolonged time period. This reflects the fact that if the characteristic fusion time is much less than the collision time, there is opportunity to enhance the coalescence process by increasing the collision rate through larger volume loading. In doing so, one essentially enhances the heat release rate by shortening the time interval between the process of cooling that a sintered particle undergoes and another collision that it encounters before cooling down completely, thereby heating up the particle even more. The corresponding primary particle sizes predicted for various volume loadings are seen in Fig. 14b. It clearly shows enhanced primary particle sizes as volume loading is increased.

4 Surface Oxidation

The fate, growth and evolution of nanoparticles leading to complex surface restructuring and reactivity, including surface oxidation, during their manufacturing via flame synthesis [117, 118] plasma processing [119] or flow reactors [120, 121] has been extensively studied. The motivation for such studies resides in the directed fabrication of nano-structured materials and thin films with controlled porosity, specific surface coatings and catalytic properties. Structural rearrangements during nanoparticle evolution can lead to the formation of either compact spherical nanoparticles with low surface area (electronic device fabrications, sensors, etc.) or, fractal-like aggregates with high surface area (nanocatalysts, energetic materials, H_2

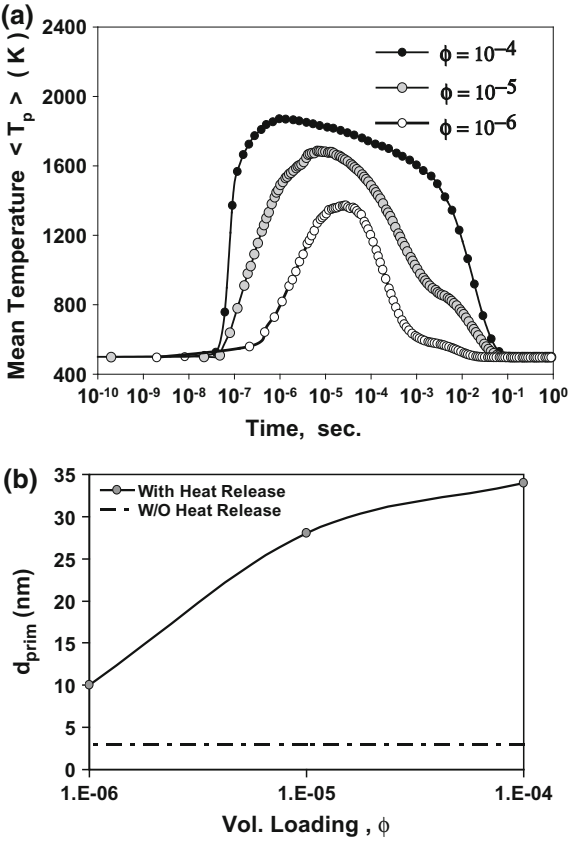

Fig. 14 Effect of different particle volume loading ($\phi = 10^{-4}, 10^{-5}, 10^{-6}$) on **a** the temporal variation of the mean particle temperature ($<T_p>$); and **b** the prediction of primary particle sizes (d_{prim}) for Si nanoparticle coalescence ($T_g = 500$ K and $P_g = 100$ Pa). Primary particle size predicted without heat release effect has also been indicated

storage, etc.). Yet, the complex interplay between the various physical pathways such as collision/coalescence as discussed in the previous sections, and chemical kinetics of their surface reactivity during gas-phase synthesis of these structures is not clearly understood.

Aerosol dynamics based sectional/ nodal models [37, 38, 122], method of moments [123, 124] or, models for particle laden flows [125, 126] have been widely used to study nanoparticle evolution in the past. But, only recently Monte Carlo (MC) based stochastic models, as developed in our earlier sections, have been able to simulate nanoparticle coagulation, aggregation, surface growth and restructuring [47, 79] without resorting to a single unifying governing multivariate equation [44]. Specifically, MC simulations of nanoparticle aggregation and restructuring via coalescence/sintering [102] have provided great insight into the role of process parameters in controlling the structures of gas-phase synthesized nanoparticles [127]. Furthermore, the highly exothermic and energetic nature of coalescence due to self-reinforcing atomic diffusions at nano-scale [39, 95] have prompted recent kinetic MC (KMC) studies to elucidate the role of non-isothermal

coalescence in tailoring the size and shape of nanoparticles generated via collision-coalescence events [44]. The implications of a competing, non-isothermal collision-coalescence event leading to complex nanoparticle shapes are far-reaching in regards to the thermal and morphological activation of the interfacial chemistry of these nanostructured materials.

The aforementioned studies have encouraged systematic characterizations of complex fractal-like structures of nano-aggregates, in lieu of the commonly used equivalent spherical shapes [128, 129]. Such modifications significantly alter the inter-particle collision frequency function [130] and hence their growth dynamics. The excess surface area of fractal-like nanostructures, when coupled with the exothermic nature of coalescence, makes the chemical physics of surface energy-driven interfacial processes such as oxidation and coagulation-coalescence in nanoparticles [131] highly complex and intriguing. Yet, to date a comprehensive study of the non-linear coupling between all of the aforementioned energetic processes in the framework of synthesizing fractal-like nano-structures has not been performed.

Understanding these complex energetic processes is essential for establishing the process guidelines for synthesis of tailored nanostructures with controlled oxide layers for surface passivation, energetic or, specific catalytic and electronic applications [132–134]. Specifically, the energetic properties of metal nanoparticles (<100 nm) with large surface-to-volume ratio and energy densities [135–137] have attracted much attention from the combustion community (e.g., solid propellant or, pyrotechnique research). To this end, oxidation kinetics of Al NPs have been investigated using thermogravimetric analysis (TGA), Rutherford backscattering spectrometry (RBS) studies [138], single particle mass spectrometry (SPMS) [139] and laser-induced breakdown spectroscopy (LIBS) [140] techniques.

Recent phenomenological models [12] and Molecular Dynamics (MD) simulations [141, 142], although simplistic in assuming spherical particle shapes, have provided critical insight into metal nanoparticle oxidation. But, due to computational limitations, they fail to account for the exothermic effects of the competing collision-coalescence processes during nanoparticle growth mechanism [44]. The motivation behind the investigations discussed in this section stems from the fact that most studies on metal nanoparticle oxidation rely on the simplified assumption of spherical particles while looking at size evolution and/or surface oxidation of single particle [12], uniformly sized particles [143] or, ensemble particle size distributions [144]. Thus, here we present our recently developed KMC model that efficiently accounts for coagulation-coalescence events coupled with particle energy balance and surface oxidation during the synthesis of metal nanoparticles with fractal-like structures under typical processing conditions dictated by background gas pressure (p_g), temperature (T_g) and material volume loading (ϕ). This model for the first time allowed the investigation of the role of morphological complexity defined by surface fractal dimensions of metal nano-aggregates in their growth mechanism, energetic activities, extents of oxidation and structural/ compositional changes. Specifically, due to the wealth of high quality experimental data [135–140], we specifically report the investigation of

gas-phase synthesis of Al nanoparticles undergoing simultaneous oxidation (i.e., Al/Al_2O_3 system) as a case study to demonstrate the efficacy of the KMC model.

4.1 Mathematical Model and Theory

4.1.1 Morphology: Surface Fractal Dimension

The present study is focused on interfacial processes such as coalescence and surface oxidation, and hence, uses the surface fractal dimension D_s [145] to describe particle morphology. Based on the scaling law relation [146] between particle surface area (A_p) and volume (V_p): $A_p \propto V_p^{D_s/3}$ for fractal-like surfaces, D_s is estimated from the slope of a linear fit to $\ln(A_p)/A_0$ vs. $\ln(V_p)/V_0$ for the ensemble particle system as per the normalized area-to-volume relationship with their primary particles [145]:

$$\frac{A_p}{A_0} = \left(\frac{V_p}{V_0}\right)^{\frac{D_s}{3}} \tag{50}$$

Theoretically, $2 \leq D_s \leq 3$, where $D_s = 2$ represents perfect smooth spheres; $2 < D_s < 3$ represents self-similar fractal-like aggregates undergoing partial coalescence and, $D_s = 3$ represents completely open-chained fractal aggregates (Fig. 15). In using Eq. 50, it needs to be mentioned that the choice of initial monomers as primary particles in the system, as used earlier [112], is not valid when collision-coalescence mediated growth ($\tau_f \ll \tau_{coll}$) generates significantly large, uniform spherical particles that act as the primary particles in newly formed aggregates. Hence, subject to a log-normal distribution of aggregates coalescing into uniform spherical particles (discussed later), log mean diameter of the particle ensemble is assigned as the characteristic primary particle dimension. At the onset of aggregation, the primary particle size estimated from the most recent particle ensemble is used for the D_s estimation of all future aggregates. In addition, the validity of Eq. 1 for $D_s > 2$ requires a substantial number of primary particles (>10–20) in any cluster to minimize error arising from the spherical primary particle morphology ($D_s = 2$).

4.1.2 Collision Kernel and Characteristic Collision Time

Based on Eqs. 3 and 30 in the earlier Sects. 2.1 and 3.1.1, the free molecular form of the collision kernel between two particles i and j of any shapes and cluster sizes, varying particle temperatures [44] and densities (due to compositional variations), can be represented as [145]:

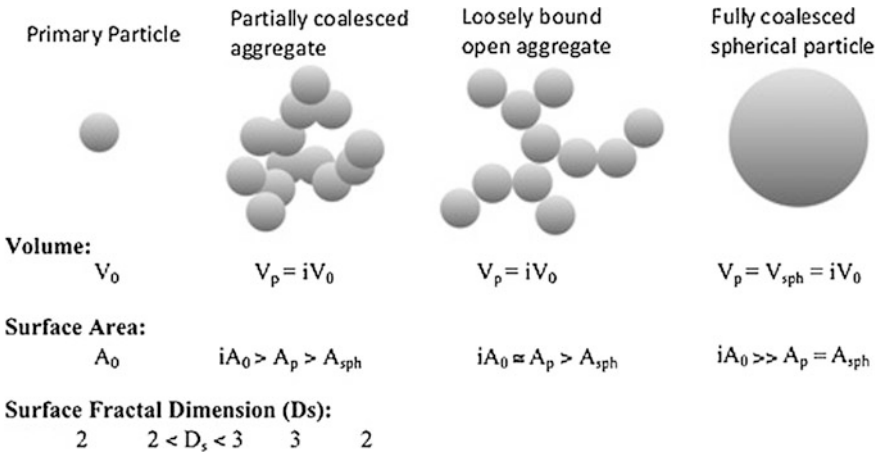

Fig. 15 Schematic indicating particle morphology variations

$$\beta_{ij} = \frac{1}{4}\left(\frac{8k_b}{\pi}\right)^{1/2}\left(\frac{T_i}{\rho_i V_i} + \frac{T_i}{\rho_j V_j}\right)^{1/2}\left[\left(s_i A_i\right)^{1/2} + \left(s_j A_j\right)^{1/2}\right]^2 \tag{51}$$

$$s_i = (D_s - 2)\left(\frac{2}{i}\right)^{1-\chi} + (3 - D_s) \tag{52}$$

where, it is noted that when $D_s = 2$ for dense spheres, $s_i = 1$ and χ is experimentally determined to be 0.92 for typical nanoparticle aggregation [147, 148].

In terms of β_{ij} (Eq. 51) and aerosol self-preserving size distribution (SPD) theory [85] based non-dimensional particle volumes, $\eta_i = N_\infty V_i/\phi$ and size distributions, $\psi(\eta_i) = N_i\phi/N_\infty^2$ (as also presented in Fig. 10 in Sect. 3.2.2.), rate of change in particle number concentration is given as:

$$\frac{dN_\infty}{dt} = -\frac{a}{2}\Omega N_\infty^{5/2} I(\eta_i, \eta_j) \text{ where, } I(\eta_i, \eta_j) = \int_0^\infty \int_0^\infty F(\eta_i, \eta_j)\psi(\eta_i)\psi(\eta_j)d\eta_i d\eta_j \tag{53}$$

and

$$F(\eta_i, \eta_j) = \left(\frac{1}{\eta_i} + \frac{1}{\eta_j}\right)^{1/2}\left[\eta_i^{\gamma/2}\left\{1 + (b\theta/a)\eta_i^{1-\chi}\right\}^{1/2} + \eta_j^{\gamma/2}\left\{1 + (b\theta/a)\eta_j^{1-\chi}\right\}^{1/2}\right]^2 \tag{53a}$$

where,

$$\Omega = \left(\frac{2k_b\overline{T}}{\pi\overline{\rho}\phi}\right)^{\frac{1}{2}}\left(\frac{A_0}{2^{\chi}\eta_0^{\gamma}}\right); \gamma = (D_s/3 + \chi - 1); a = (D_s - 2); b = (3 - D_s); \theta = (2\eta_0)^{\chi-1}$$

$\eta_0 = N_\infty V_0/\phi$ The volume integral over the entire population in Eq. 53 justifies the use of an ensemble averaged particle density and temperature, $\bar{\rho}$ and $\overline{T}$, whereas the statistical nature of the problem provides support for the use of D_s, obtained from the linear fit of Eq. 50 over the particle ensemble, to represent the surface morphology of individual particles.

Here $I(\eta_i, \eta_i)$, which has been numerically solved for homogeneous forms of $F(\eta_i, \eta_j)$ at different volume fractal dimensions [85] (D_f), becomes analytically intractable and numerically intensive due to the non-homogeneous form of $F(\eta_i, \eta_j)$ in Eq. 53a. Thus, asymptotic solutions of $\left\{1 + (b\theta/a)\eta_i^{1-\chi}\right\}^{1/2} \cong 1$ when, $(b\theta/a) \ll 1$ $(D_s \to 2)$ and $\left\{1 + (b\theta/a)\eta_i^{1-\chi}\right\}^{1/2} \cong (b\theta/a)^{1/2}\eta_i^{1-\chi/2}$ when,$(b\theta/a) \gg 1$ $(D_s \to 3)$ (Note: $(b\theta/a)$ ranges over several orders of magnitude, whereas $\eta_i^{1-\chi} \sim 0.5 - 1.0$) lead to the homogenous forms of $I(\eta_i, \eta_j)$. Upon numerical integration, $I(\eta_i, \eta_j)$ converges to the average values $\sim$ 6.576 and 6.577 over the respective ranges of D_s = 2.4–3.0 and D_s = 2.0–2.6 (see Table 2). Finally, using an average value of $I(\eta_i, \eta_j) = 6.577$ in Eq. 53, the characteristic collision time τ_{coll} (time taken by a particle to double its volume and hence, N_∞ to drop to $N_\infty/2$ via coagulation) in the respective D_s regimes is estimated from:

$$\tau_{coll} = \frac{N_\infty^{(\gamma-3/2)}\left(1 - 0.5^{(\gamma-3/2)}\right)}{Ya(\gamma - 3/2)I(\eta_i, \eta_j)} \quad \text{for } D_s \to 3 \text{ (approaching fractal)} \tag{54}$$

$$\tau_{coll} = \frac{N_\infty^{(\gamma-\chi-1/2)}\left(1 - 0.5^{(\gamma-\chi-1/2)}\right)}{Yb(\gamma - \chi - 1/2)\left(\frac{2V_0}{\phi}\right)^{\chi-1}I(\eta_i, \eta_j)} \quad \text{for } D_s \to 2 \text{ (approaching sphere)} \tag{55}$$

where, the intermediate coefficient,

$$Y = -\frac{1}{2}\left(\frac{2k_b\overline{T}}{\pi\overline{\rho}\phi}\right)^{\frac{1}{2}}\left(\frac{A_0}{2^{\chi}}\right)\left(\frac{\phi}{V_0}\right)^{\gamma}. \tag{56}$$

The final τ_{coll}, as constructed from Eqs. 5 and 6 in the respective particle morphology regimes of $D_s \to 2$ (earlier times) and $D_s \to 3$ (later times), exhibit the

Table 2 Numerical values of the integral $I(\eta_i, \eta_j)$ in Eq. 4 for $D_s \rightarrow 2$ and $D_s \rightarrow 3$[a]

D_s	2.0	2.1	2.2	2.3	2.4	2.5	2.6	2.7	2.8	2.9	3.0	Mean
$I(\eta_i, \eta_j)$ $D_s \rightarrow 3$	6.739	6.702	6.657	6.624	6.576	6.578	6.569	6.546	6.576	6.572	6.615	6.576
$I(\eta_i, \eta_j)$ $D_s \rightarrow 2$	6.624	6.576	6.578	6.569	6.546	6.576	6.572	6.615	6.651	6.694	6.744	**6.577**

[a]Adapted from *AIChE J., 58, 3341 (2012)* [49] with copyright permission from Wiley

expected escalation in τ_{coll} at later stages due to larger collision cross-sections of fractal-like aggregates.

4.1.3 Coalescence

Coalescence can be approximated by the Eq. (34) in Sect. 3.1.2 to model the surface area reduction rate [85]. In this case, the variations in mean characteristic fusion time, τ_f (i.e., time needed to reduce the excess agglomerate surface area, $\left(A_p - A_{sph}\right)$ by 63%) has to be accounted for due to the formation of composite phase segregated nanoparticles as a result of metal (M) → metal oxide (MO_x) phase transitions. In doing so, τ_f is estimated from individual $\tau_{f(M)}$ and $\tau_{f(MOx)}$ weighted by respective metal (M)/metal oxide (MOx) volume fractions:

$$\tau_f = \tau_{f(M)}^{\varphi_M} \tau_{f(MOx)}^{\varphi_{MOx}} \tag{57}$$

to account for the predominant diffusion rates due to dynamical variations in the M and MOx composition within the particle. Depending on particle temperatures T_p, melting points $T_{m(x)}$ and physical states of material, individual $\tau_{f(x)}$ (x = M or, MOx) are calculated as: (1) $\tau_{f(x)} = \frac{3k_b T_p n_x}{64\pi\sigma_S(x) D_{eff}}$ for grain boundary diffusion (solid state sintering when $T_p < T_{m(x)}$ [98]) where, D_{eff} is the effective diffusion coefficient [44] ($m^2\ s^{-1}$) and, (2) $\tau_{f(x)} = \frac{\mu_x d_{p(eff)}}{2\sigma_{l(x)}}$ for viscous diffusion (molten state liquid sintering when $T_p \geq T_{m(x)}$ [102]) where, $d_{p\,(eff)} = 6V_p/A_p$ accounts for multiple sintering necks on one particle [44].

$T_{m(x)}$ (x = M or, MOx), being highly sensitive to particle sizes (d_p) at nano-scale, is determined from the expression for size-dependent melting point of nanomaterials [149]:

$$T_{m(x)}\left(d_p\right) = T_{b(x)}\left\{1 - \frac{4}{h_L \rho_{s(x)} d_p}\left[\sigma_{s(x)} - \sigma_{l(x)}\left(\frac{\rho_{s(x)}}{\rho_{l(x)}}\right)^{2/3}\right]\right\} \tag{58}$$

The respective thermochemical and physical properties used in Eq. 58 are specifically reported in Table 3 for the Al/Al_2O_3 case-study.

4.1.4 Surface Oxidation: Transport Model and Species Balance

The surface oxidation model has the following features: (1) Uniform oxide shell formation, based on the *shrinking core like model* [150], hence the core shrinks in size while maintaining the same morphology (given by D_s) as the external particle surface (Fig. 16); (2) Only surface oxidation of solid and liquid material leads to solid oxide (ash) formation; (3) O_2 diffuses through the ash layer to oxidize the

Table 3 Thermochemical and physical properties of Al and Al_2O_3[a]

Properties	AL (Ref.)	Al_2O_3 (Ref.)
Solid density, $\rho_{S(X)}$ (kg/m^3)	2700 [151]	3980 [151]
Solid surface tension, $\sigma_{s(X)}$ (J/m^2)	1.14 [151]	1.12 [151]
Liquid density, $\rho_{l(X)}$ (kg/m^3)	2377 [152]	2930 [153]
Liquid surface tension, $\sigma_{l(X)}$ (J/m^2)	1.05 [154]	0.64 [153]
Molecular weight (g/mol)	27	102
Molar volume, v_{mol} (m^3/mol)	1×10^{-5}	2.56×10
Heat of vaporization, h_v (kJ/mol)	294 [151]	346.94 [155][b]
Latent heat of melting, h_L (kJ/mol)	10.7 [151]	109 [153]
Heat capacity, $c_{p(X)}$ [J/(kg°C)]	917 [151]	775 [151]
Bulk melting point, $T_{m(X)}$ (K)	933[151]	2327[151]
Viscosity, μ_x (Pa-s)	$4.97 \times 10^{-4}\ [T_m/(T_p - T_m)^{0.5714}$ [156]	$(3.2 \times 10^{-3}) \exp[4.32 \times 10^4/(R_u T_p)]$ [153]
Grain boundary diffusion coefficient, D_{GB} (m^2/s)	$(\alpha/\delta) \exp[-\beta/(R_u T_p)]$ [151]	$(\alpha/\delta) \exp[-\beta/(R_u T_p)]$ [151]
δ: Grain boundary width = 0.5 nm	$\alpha = 3 \times 10^{-14}$ m^2/s; $\beta = 6 \times 10^4$ J/mol	$\alpha = 3 \times 10^{-3}$ m^2/s; $\beta = 4.77 \times 10^5$ J/mol
Saturated vapor pressure, p_{sat} (Pa)	$\exp(13.07 - 36,373/T_p)$ [12]	$101325.\exp(13.42 - 27,320/T_p)$ [157]
Other thermochemical properties		
Enthalpy of reaction (kJ/mol)	2324 [139]	
Temperature dependent surface tension (N/m)	$\sigma_{Al}(T_p) = 0.001[860 - 0.134(T_p - 933)]$ [158]	
Thermal conductivity of Al_2O_3, k_{ash} [W/(m-K)]		$\alpha + \beta \exp[-\gamma(T_p - \theta)]/[(T_p - \theta) + \varepsilon]$ [159] $\alpha = 5.85;\ \beta = 15,360;\ \gamma = 0.002;\ \theta = 273.13$
First-order reaction rate coefficient, k_f (m/s) $d_p < 50$nm $50\text{nm} < d_p < 100\text{nm}$ $100\text{nm} < d_p$	$24.\exp[-31.8 \times 10^3/(R_u T_p)]$ $180.\exp[-56.9 \times 10^3/(R_u T_p)]$ $(5.4 \times 10^7)\exp[-174.6 \times 10^3/(R_u T_p)]$ [139]	

(continued)

Table 3 (continued)

Properties	AL (Ref.)	Al_2O_3 (Ref.)
Heterogeneous diffusion coefficient (m^2/s)	$\mathbf{O_2 \rightarrow Al_2O_3}$ $D_{O_2\|Ash} = \alpha \exp\left[-\beta/\left(R_u T_p\right)\right]$ [139] $\alpha = 1.72 \times 10^{-9}\ m^2/s;\ \beta = 69.5\ J/mol$	$\mathbf{Al_2 \rightarrow Al_2O_3}$ $D_{Al_2\|Ash} = \alpha \exp\left[-\beta/\left(R_u T_p\right)\right]$ [157] $\alpha = 2.8 \times 10^{-3}\ m^2/s;\ \beta = 477.3\ J/mol$

[a]Adapted from *AIChE J., 58, 3341 (2012)* [49]

[b]h_v (kJ/mol) for Al_2O formation is considered by assuming the pathway for Al_2O_3 evaporation as: $4/3\ Al + 1/3\ Al_2O_3 \rightarrow Al_2O(g) \rightarrow 2Al\,(g) + 1/2\ O_2(g)$; [155]

metal at shell-core interface (Fig. 16); (4) Molten metal from unreacted core diffuses in opposite direction through the ash layer to react with O_2 at particle surface (Fig. 16); (5) Pressure gradient in nanoparticle core opposing the inward diffusion of O_2 and resulting in rupturing or thinning of ash layer [12] is not considered; (6) D_s driven shape parameter factors account for particle morphology.

The Damköhler number (Da) determines the relative roles of reaction ($Da \ll 1$) or, diffusion limited ($Da \gg 1$) oxidation mechanisms. It is defined for reacting species (m = O_2 or, metal) diffusing through mediums (n = gas film or, ash layer) as:

$$Da_{(m|n)} = \frac{\tau_{diff(m|n)}}{\tau_{rxn}} \tag{59}$$

Characteristic reaction time τ_{rxn} for surface oxidation of nanoparticles is defined as:

$$\tau_{rxn} = \frac{1}{\zeta_{SV} k_f(T, d_p)} \tag{60}$$

where, $\zeta_{SV} = A_p/V_p$ is surface-to-volume ratio (m^{-1}) and $k_f(T, d_p)\ \left[\sim \alpha_{oxid} \exp\left(-E_{oxid}/k_b T_p\right)\right]$ is the temperature and size (based on Al nanoparticle oxidation studies in size regimes of: <50 nm, 50–100 nm and >100 nm [139]) dependent first-order reaction rate coefficient (see Table 3). Characteristic diffusion time $\tau_{diff(m|n)}$ for species, m diffusing through medium, n is defined as:

$$\tau_{diff(m|n)} = \frac{1}{\zeta_{SV}^2 D_{(m|n)}} \tag{61}$$

In this study, the following oxidation routes are considered:

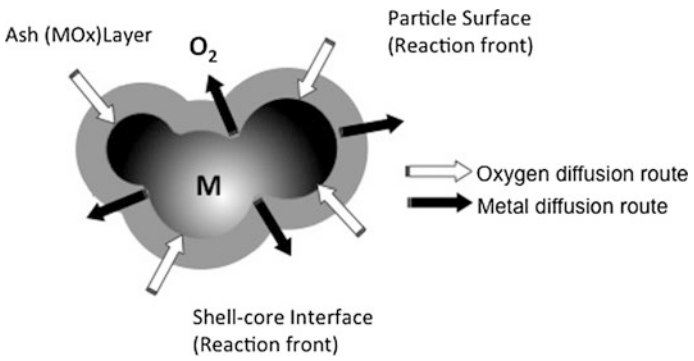

Fig. 16 Schematic for shell-core oxidation model

a. Bare metal particle: Diffusion of O_2through the gas film: For all cases studied, characteristic $Da_{(O_2|Gas)} \ll 1$ (where $\tau_{diff(O_2|Gas)}$ is determined from Eq. 61 using $D_{O_2|Gas}$) for O_2 diffusion to the bare particle surface indicates the process to be always reaction controlled. Hence, the reaction rate is expressed as:

$$\dot{\omega}_{O_2|Gas} = -\frac{dn_{O_2}}{dt} = A_p k_f C_{O,\infty} \tag{62}$$

b. Oxide coated particle: Oxide shell formation prompts the following parallel processes: (i) *Diffusion of O_2through oxide shell to core surface:* Net oxidation rate, mainly governed by the reaction at the *core metal surface* (Fig. 16), is derived as:

$$\dot{\omega}_{O_2|Ash} = -\frac{dn_{O_2}}{dt} = \frac{A_p k_f C_{O,\infty}}{1 + \frac{Da_{(O_2|Ash)}}{Z_{O_2}}} \tag{63}$$

and, (ii) *Diffusion of molten metal through oxide shell to particle surface:* Net oxidation rate, mainly governed by the reaction at the *particle surface* (Fig. 17), is derived as:

$$\dot{\omega}_{M|Ash} = -\frac{dn_M}{dt} = \frac{A_p k_f C_{M,c}}{1 + \frac{Da_{(M|Ash)}}{Z_M}} \tag{64}$$

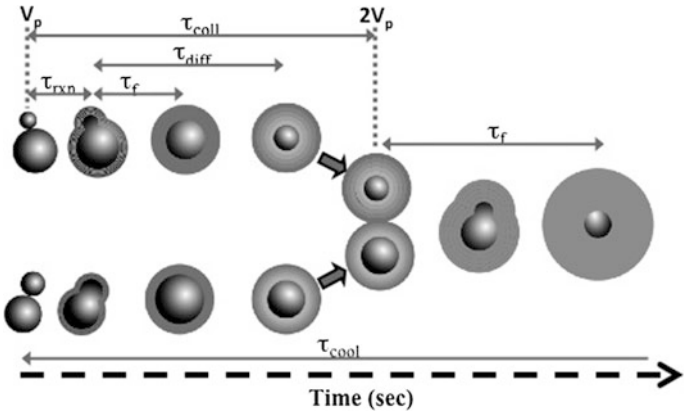

Fig. 17 Schematic of the relative time scales of events during nanoparticle synthesis undergoing surface oxidation and simultaneous collision-coalescence processes where in for typical energetic oxidation processes: $\tau_{cool} > \tau_{coll} > \tau_f > \tau_{diff} > \tau_{rxn}$

Equations 63 and 64 are derived using the scaling law relations: $A_p/A_c = \left(V_p/V_c\right)^{D_s/3}$ (self-similar shrinking core assumption in feature 1 above and Fig. 16) between the particle and its core surface area and volume such that the morphological complexity are accounted for through the non-dimensional shape parameters: $Z_{O_2} = \sqrt{\frac{4\pi}{A_p}}\frac{\lambda^2}{\zeta_{SV}(\lambda-1)}$ (for O_2 diffusing out through the ash layer) and $Z_M = \frac{1}{\lambda^2}Z_{O_2}$ (for metal diffusing in through the ash layer) along with $\lambda = \left(V_p/V_c\right)^{D_s/6}$. The boundary conditions used for O_2 concentrations [150] in Eq. 63 are: $C_o\left(A_p\right) = C_{o,\infty}$; $C_o(A_c) = 0$ while those for the metal concentrations in Eq. 64 are: $C_M(A_c) = C_{M,c}$; $C_M\left(A_p\right) = 0$. Characteristic $Da_{(O_2|Ash)}$ (O_2 diffusion through the ash layer) and $Da_{(M|Ash)}$ (metal diffusion through the ash layer) are calculated from Eqs. 59 and 60 using the respective $\tau_{diff(O_2|Ash)}$ and $\tau_{diff(M|Ash)}$ (Eq. 61) as estimated from $D_{O_2|Ash}$ and $D_{M|Ash}$. It is noted that Eqs. 63 and 64, by their mechanistic design, shall drive the oxidation to be reaction limited or, diffusion limited based on the expressions: $\frac{Da_{O_2|Ash}}{Z_{O_2}}$ and $\frac{Da_{M|Ash}}{Z_M}$ being $\ll 1$ or, vice versa respectively.

Specifically, for the Al/Al_2O_3 case-study used here to discuss the results obtained from the present model, the extent of conversion α (i.e., amount of Al converted to Al_2O_3) is defined as [139, 140, 150]:

$$2Al + \frac{3}{2}\alpha O_2 \rightarrow (1-\alpha)Al + \alpha Al_2O_3 \text{ where, } \alpha = \frac{2n_{Al_2O_3}}{2n_{Al_2O_3} + n_{Al}} \tag{65}$$

Finally, the stoichiometric species balance results in the net oxidation rate as:

$$\dot{\omega}_{O_2} = \dot{\omega}_{O_2|Ash} + \frac{3}{4}\dot{\omega}_{Al|Ash} \tag{66}$$

Also, to account for compositional changes, mean particle density, ρ_p and surface tension, σ_p used throughout the simulations for the Al/Al_2O_3 system are estimated as:

$$\rho_p = \varphi_{Al}\rho_{Al} + \left(1-\varphi_{Al_2O_3}\right)\rho_{Al_2O_3}$$
$$\sigma_p = \varphi_{Al}\sigma_{Al} + \left(1-\varphi_{Al_2O_3}\right)\sigma_{Al_2O_3}$$

where, ρ_{Al} and $\rho_{Al_2O_3}$ are taken to be the bulk solid densities: $\rho_{s(Al)}$ and $\rho_{s(Al_2O_3)}$, whereas surface tension of Al, σ_{Al} is calculated from σ_{Al} (T_p) and $\sigma_{(Al_2O_3)}$ is taken as $\sigma_{s(Al_2O_3)}$ or, $\sigma_{1(Al_2O_3)}$ for $T_p < T_{m(Al2O3)}$ or, vice versa respectively (refer to Table 3).

4.1.5 Energy Balance

The net rate of bulk energy increase E_p, in a nanoparticle/aggregate due to coalescence and oxidation, compensated by the rate of heat losses by conduction and evaporation (radiation being negligible in nano-sized particles [44]) is given as:

$$\frac{dE_p(T_p)}{dt} = \left(m_M c_{p(M)} + m_{MOx} c_{p(MOx)}\right)\frac{dT_p}{dt} = \dot{E}_{coal} + \dot{E}_{oxid} - \dot{E}_{cond} - \dot{E}_{evap} \quad (67)$$

$\dot{E}_{coal}$, based on coalescence rate (Eq. 34) for surface energy reduction, is given as [44]:

$$\dot{E}_{coal} = -\sigma_p \frac{dA_p}{dt} = \frac{\sigma_p}{\tau_f}\left(A_p - A_{sph}\right) \quad (68)$$

$\dot{E}_{oxid}$ is calculated from oxygen consumption rate $\dot{\omega}_{O_2}$ obtained from Eq. 66 as:

$$\dot{E}_{oxid} = \dot{\omega}_{O_2}\frac{H^{o}_{rxn}}{N_{av}} \quad (69)$$

where, H^{o}_{rxn} is the enthalpy of metal oxidation (kJ mol^{-1}).

$\dot{E}_{cond}$ for the rate of heat loss via conduction is given as:

$$\dot{E}_{cond} = \frac{R_{kin}\left(T_p - T_g\right)}{1 + \left(\frac{R_{kin}}{R_{Ash}}\right)} \quad (70)$$

where, $R_{Ash} = k_{ash}\frac{\sqrt{4\pi A_P}}{\lambda - 1}$ is the resistance term for heat conduction through the ash layer whereas, $R_{Kin} = m_g c_g \frac{p_g A_p}{\sqrt{2\pi m_g k_b T_g}}$ accounts for collisions with gas molecules at the particle surface as derived from kinetic theory [44]. Here, the assumption of lumped heat in the metal core is valid for $c_{p(M)} > c_{p(MOx)}$.

Finally, $\dot{E}_{evap}$ for the rate heat loss via evaporation is formulated as:

$$\dot{E}_{evap} = \frac{\varepsilon_{kin}(h_v/N_{av})A_p}{1 + \left(\frac{\varepsilon_{Kin}}{\varepsilon_{Diff}}\right)} \quad (71)$$

where, $\varepsilon_{Diff} = D_{M|Ash} C_{M,c}\frac{\sqrt{4\pi A_P}}{\lambda - 1}$ is the contribution from molten core metal diffusing through ash layer which competes with $\varepsilon_{Kin} = \frac{p_{drop}}{\sqrt{2\pi k_b T_p m_M}}$ due to evaporation of the molten metal from particle surface [12] where vapor pressure on a droplet is related to that on a flat surface at temperature, T_p via Kelvin relation:

$$p_{drop} = p_{sat}(T_p)\exp\left(\sqrt{\frac{\pi}{A_p}}\frac{4\sigma_p v_{mol}}{R_u T_p}\right) \tag{72}$$

For completely oxidized particles, $\dot{E}_{evap}$ is calculated from the ε_{Kin} term only based on h_v, p_{drop} and p_{sat} of pure metal oxide. The temperature ranges in the present study makes oxide shell evaporation, although built into the model as a safeguard against exceedingly high particle temperatures, negligible due to the fact that $T_{mp(M)} \ll T_{mp(MOx)}$ as well as p_{sat} being extremely low for most metal oxides. All thermochemical and physical properties used in the aforementioned equations for the simulation of Al/Al_2O_3 system in the present study are charted out in Table 3. All notations used here are reported at the end of the article.

4.2 Modeling Surface Oxidation: Coagulation Driven KMC Model

The KMC model presented here is built on the earlier coagulation driven constant-number (*constant-N*) MC with periodic boundary conditions as developed in [112] and described in details in the previous Sect. 3.2. As also mentioned before, the current MC algorithm operates based on the probability of occurrence of a coagulation (p_{ij}) event as represented by Eq. 49 under Sect. 3.2, wherein the MC particles undergoing coagulation are replenished by replicating the system with copies of the surviving particles whenever the particle number drops to 50% of the initial number, thereby enabling a computationally efficient method without loss of accuracy. Here the $\beta_{max} = f(V_p, \rho_p, T_p, D_s)$, as per Eq. 51, is estimated from all particles in the system. At any step, for $p_{ij} \geq R \in [0, 1]$, a collision event between two randomly chosen particles (i and j) is accompanied by an advancement of the MC time-step ΔT_{MC} (mean inter-event time between successive coagulations), as calculated from the inverse of the sum of the rates of all possible collision events and represented by Eqs. 44–46 in the previous Sect. 3.2.

Here in simulating the surface of the fractal-like aggregates, within each ΔT_{MC}, Eqs. 34 and 62 [bare metal particles] or, 66 [oxide coated particles] and 67 are numerically solved for coalescence, oxidation and energy/species conservations for the ensemble particles. The schematic in Fig. 17 elucidates the characteristic time scales governing the inter-play between the aforementioned processes i.e., collision (τ_{coll}), fusion (τ_f) and diffusion (τ_{diff}) or, reaction (τ_{rxn}) limited oxidation in relation to the characteristic time taken to quench the energetic processes in a particle (τ_{cool}). To capture the real physico-chemical processes, the rate-determining characteristic time, τ_{Char} is taken as the fastest amongst τ_{coll}, τ_f, τ_{diff} and τ_{rxn}, and it is used as the time step Δt within each ΔT_{MC} as:

$$\Delta t = \frac{\Delta T_{MC}}{k_{max}} \text{ where, } k_{max} = \frac{\Delta T_{MC}}{\tau_{Char}} \times k \tag{73}$$

where, k_{max} is the number of iteration loops for the numerical integrations ($k \sim 10$, or 100 to ensure accuracy). Typical particle temperature profiles obtained from simulations with $N_{MC} = 5000$ and 10,000 showed negligible variations. Since the computational time for 5000 particles is $\sim$3 days as compared to $\sim$3–5 weeks for 10,000 particles, all results presented henceforth are for $N_{MC} = 5000$ particles.

4.3 Effect of Morphology and Non-isothermal Coalescence on Surface Oxidation of Metal Nanoparticles: Results from the Study

All results presented here are for the representative case-study of the oxidation and evolution of Al/Al_2O_3 nanoparticles during gas-phase synthesis.

4.3.1 Estimation of Primary Particle Size

For the estimation of the mean primary particle size, the particle ensemble is assumed to be "mostly spherical" when the ensemble averaged normalized excess surface area $\left\langle \left(A_p - A_{sph}\right)/A_{sph} \right\rangle < 0$. As an example, for $T_g = 800$ K, the primary particle size is fixed at $t = 7.52 \times 10^{-5}$ s when $\left\langle \left(A_p - A_{sph}\right)/A_{sph} \right\rangle > 0$ (Fig. 18a) which corresponds to the crossing point between τ_f and τ_{coll} marking the onset of aggregation [85] such that spherical particles formed for $\tau_f \ll \tau_{coll}$ constitute the aggregates formed when $\tau_f > \tau_{coll}$ (collisions faster than coalescence). Keeping in mind that the slow approach of τ_f towards τ_{coll} ($d\tau_f/dt \ll d\tau_{coll}/dt$) at the crossing point might lead to the formation of oblong particles with long necks [44] we strictly use $\left\langle \left(A_p - A_{sph}\right)/A_{sph} \right\rangle > 0$ as the criterion for primary particle size selection to ensure the choice of spherical primary particles only. Furthermore, due to periodic boundary conditions, sufficient collisions ensure a log-normal distribution for the uniform spherical particles formed before the onset of aggregation, beyond which the log-mean diameter of the most recent particle distributions is fixed as the primary particle size for the rest of the particle evolution study. This is corroborated by the probability distribution function of particle sizes in Fig. 18b at $t = 7.5 \times 10^{-5}$ s (corresponding to $\left\langle \left(A_p - A_{sph}/A_{sph}\right) \right\rangle \geq 0$ in Fig. 18a indicating a log-normal distribution with estimated log-mean diameters of $\langle d_{prim} \rangle \sim 3.8$ nm ($\sigma_g = 1.93$) which is commensurate with $\langle d_{prim} \rangle$ (marked on Fig. 18a) used as the primary particle size (A_0, V_0) for the future particle evolution studies.

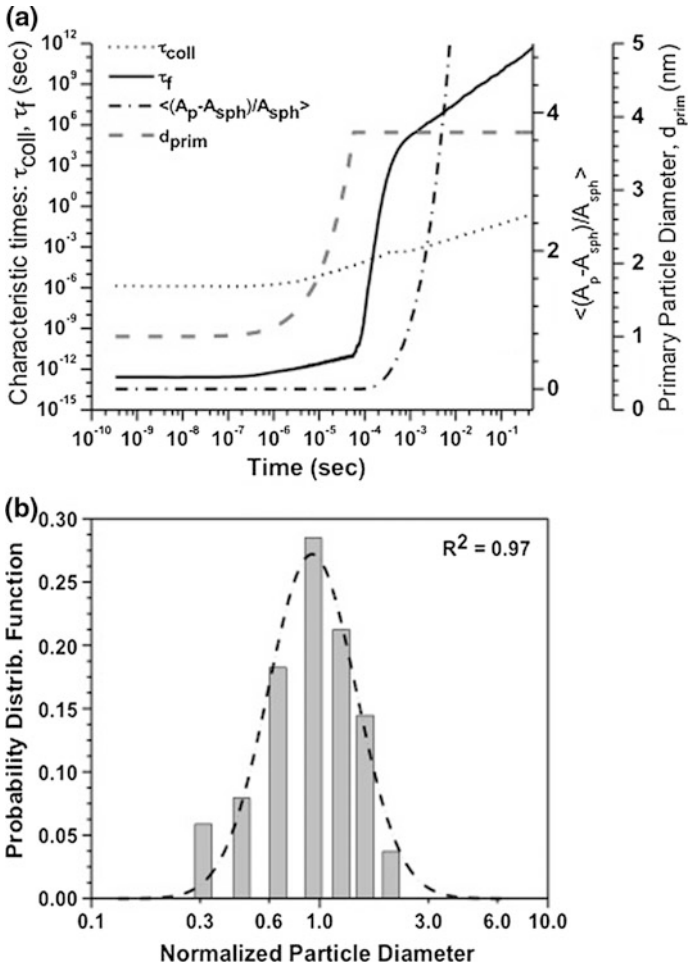

Fig. 18 **a** Determination of primary particle size, d_{prim} (nm) corresponding to cross-over point of characteristic fusion (τ_f) and collision (τ_{coll}) times; **b** Corresponding probability distribution function of primary particle sizes along with a peak fit indicating that the primary particles follow log-normal distribution with $<d_{prim}> \sim 3.8$ nm and $\sigma_g = 1.93$ ($T_g = 800$ K; $p_g = 1$ atm and $\varphi = 10^{-6}$)

4.3.2 Estimation of Particle Morphology

Using A_0 and V_0 in Eq. 50, $D_s = 2.35$ and 2.94 at two different stages of particle evolution are estimated from the slopes of the two typical linear fits to $\ln(A_p/A_0)$ versus $\ln(V_p/V_0)$ plots (Fig. 19) for $T_g = 800$ K, $p_g = 1$ atm and $\phi = 10^{-6}$. The temporal variation of D_s in Fig. 20 depicts the particle morphology evolution in relation to the different characteristic time scales τ_f, τ_{coll}, τ_{rxn} and $\tau_{diff(O_2|Ash)}$ for the

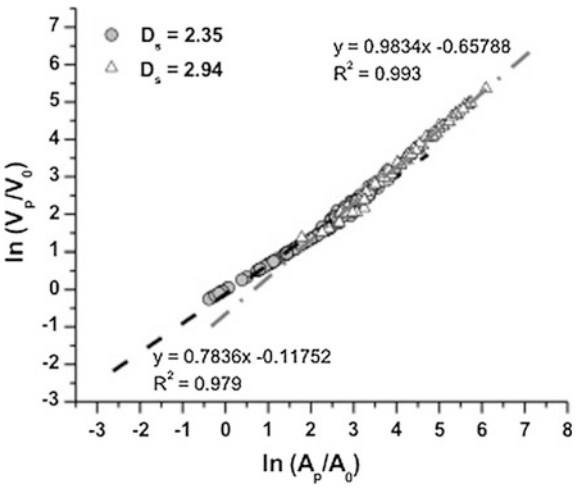

Fig. 19 Typical plots of ln (V_p/V_0) vs $\ln(A_p/A_0)$ indicating good linear fits used to determine D_s from their slopes as described by Eq. (3). Representative case studied for T_g = 800 K, p_g = 1 atm and $\varphi = 10^{-6}$

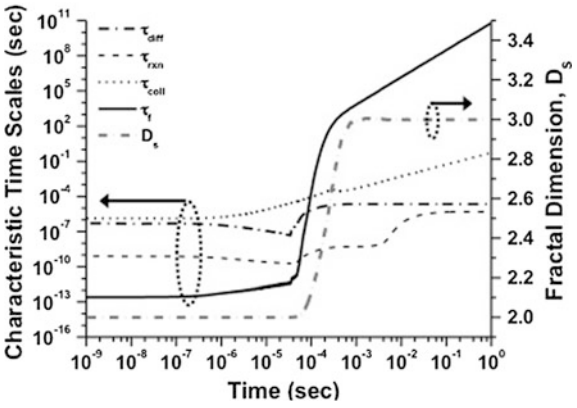

Fig. 20 Temporal evolution of typical characteristic times, τ_f, τ_{coll}, τ_{rxn} and $\tau_{diff(O_2|Ash)}$ and the significance of their cross-over points with respect to the fractal dimension, D_s of nanoparticles studied at Tg = 800 K; pg = 1 atm and $\varphi = 10^{-6}$

aforementioned operating conditions. Rapid coalescence at initial times, as compared to collision, oxidation due to surface reaction or, diffusion through the ash layer ($\tau_f \ll \tau_{coll}$, τ_{rxn} or $\tau_{diff(O_2|Ash)}$), generates spherical particles (D_s = 2). But hard oxide shell formation slows down self-diffusion, and hence coalescence. Thus, the particles transition from the molten viscous to the solid state diffusion regime as τ_f rapidly crosses τ_{rxn} and $\tau_{diff(O_2|Ash)}$ followed by τ_{coll}, hereby quenching the exothermic coalescence-oxidation processes. Corresponding to these crossing points D_s rapidly deviates from 2 (spheres) towards $D_s > 2$ (non-spherical) leading to aggregate formations ($D_s \sim 3$ at later stages in Fig. 20). At lower T_g cases, surface oxidation due to extremely retarded metal diffusion through oxide layer is negligible.

4.3.3 Surface Oxidation and Evolution of Fractal-like Al/Al_2O_3 Nanoparticles

Simulation results presented in this section are based on the case studies from Mukherjee et al.'s study [44] depicting typical laboratory or, industrial gas-phase synthesis of Al nanoparticles under standard processing conditions of: T_g = 400, 600, 1000, 1400 K; p_g = 0.1 and 1 atm; and $\phi = 10^{-6}$ and 10^{-8}. Specifically, here we will focus on the case studies for varying background gas temperatures (T_g) to elucidate the role of exothermic coagulation/coalescence mediated surface oxidation on the energetic behavior of fractal-like nano-aggregates. For further details on similar studies describing the role of other processing parameters such as gas pressure and volume loadings, the readers can refer to Mukherjee et al.'s [44] work. Unless mentioned otherwise, all simulation results presented here are for the MC system with initial particle diameters, d_{ini} = 1 nm in 5000 particles system.

In contrast to the previous coalescence studies [44] the non-linear energetic coupling between coalescence and oxidation is manifested here through the drastic rise in mean particle temperature $<T_p>$ for T_g = 400 K giving rise to the unique bi-modal temperature profiles for T_g = 1000 and 1400 K (Fig. 21a). An early rise in $<T_p>$ (bold arrow in Fig. 21a) is followed by a subsequent reduction and the formation of a second peak that finally equilibrates to T_g. In early stages, higher T_g promotes thermally activated processes such as: (1) non-isothermal coalescence due to competing collision-coalescence events ($\tau_f \ll \tau_{coll}$ in Fig. 21b) and (2) O_2 and molten Al (in this case) diffusion through relatively thin oxide layers. Specifically, when $<T_p> > 1000$ K, enhanced Al diffusion promotes rapid oxidation leading to hard oxide shell formation, which, in turn, retards coalescence and results in the temporary reduction of $<T_p>$. But the oxide shell insulation also retards conductive and evaporative heat losses from the Al core which, for small cluster sizes (d_{prim} = 4.7 and 8.4 nm for T_g = 1000 and 1400 K respectively from Fig. 21b), activate a second heat release mechanism dominated by the combined metal-metal oxide sintering (Fig. 21a and $\tau_f \ll \tau_{coll}$ in Fig. 21b). Thick oxide shells hinder both Al and O_2 diffusion and quench coalescence ($\tau_f > \tau_{coll}$ in Fig. 21b) through the final oxidation stages. Eventually, fractal-like structures with large surface-to-volume ratio, ζ_{SV} (Fig. 22) promote evaporative and conductive heat losses that relax $<T_p>$ back to T_g.

In relation to the sequence of aforementioned events, the morphological evolution (Fig. 22a) indicates that increasing T_g delays the cross-over points between τ_f and τ_{coll}. This concurs with the formation of non-spherical clusters ($D_s > 2$) with larger d_{prim} (Fig. 21b) and lower ζ_{SV} (Fig. 22a). While an earlier onset of fractal-like structures ($D_s > 2$) coincides with the peak in $<T_p>$ for T_g = 400 K, particles continue to coalesce into spheres ($D_s = 2$) until the second peak in $<T_p>$ (Fig. 21a) for T_g = 1000 and 1400 K. Finally, fractal-like aggregates ($D_s = 3$) form to reduce ζ_{SV} to a constant lower bound value except for T_g = 1400 K, where $d\tau_f/dt \approx d\tau_{coll}/dt$ (see Fig. 21b) promotes the formation of partially sintered non-spherical particles ($D_s < 2.25$ in Fig. 22a).

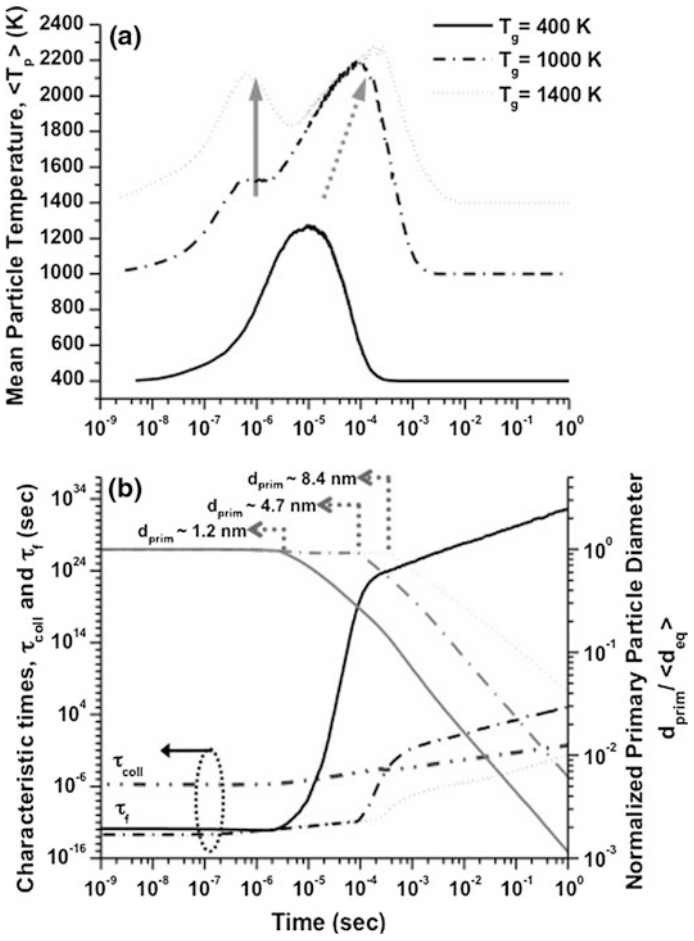

Fig. 21 Temporal variation of **a** mean particle temperatures, $<T_p>$ and **b** characteristic collision (τ_{coll}), fusion (τ_f) times (*black lines*; left Y-axis) and primary particle diameters normalized by volume equivalent diameters, $d_{prim}/<d_{eq}>$ (*gray lines*; right Y-axis) for T_g = 400, 1000 and 1400 K (p_g = 1 atm and $\varphi = 10^{-6}$). Corresponding d_{prim} values when $d_{prim}/<d_{eq}> > 1$ for each of the T_g cases are indicated

In Fig. 22b, the extent of oxidation, α for T_g = 400 K indicates that spherical particles (D_s = 2) oxidize until 4×10^{-6} s (Fig. 22a) to form a critical shell (α = 0.3 in Fig. 22b), beyond which partially sintered non-spherical particles with excess surface area ($D_s \sim$ 2–2.5 in Fig. 22a) drive α to a maximum (α = 0.59 and $d\alpha/dt \approx 0$ in Fig. 22b). But for T_g = 1000 and 1400 K, subsidence of the first peak in $<T_p>$ (Fig. 21a) in unison with α = 0.3 (Fig. 22b) indicates surface oxidation as the dominant exothermic contributor until this point. In the later stages, the formation of spherical particles (D_s = 2) until $\sim 10^{-4}$ s (Fig. 22a) implies a dominant coalescence (as discussed earlier), wherein most of the oxidation (> 85%) has

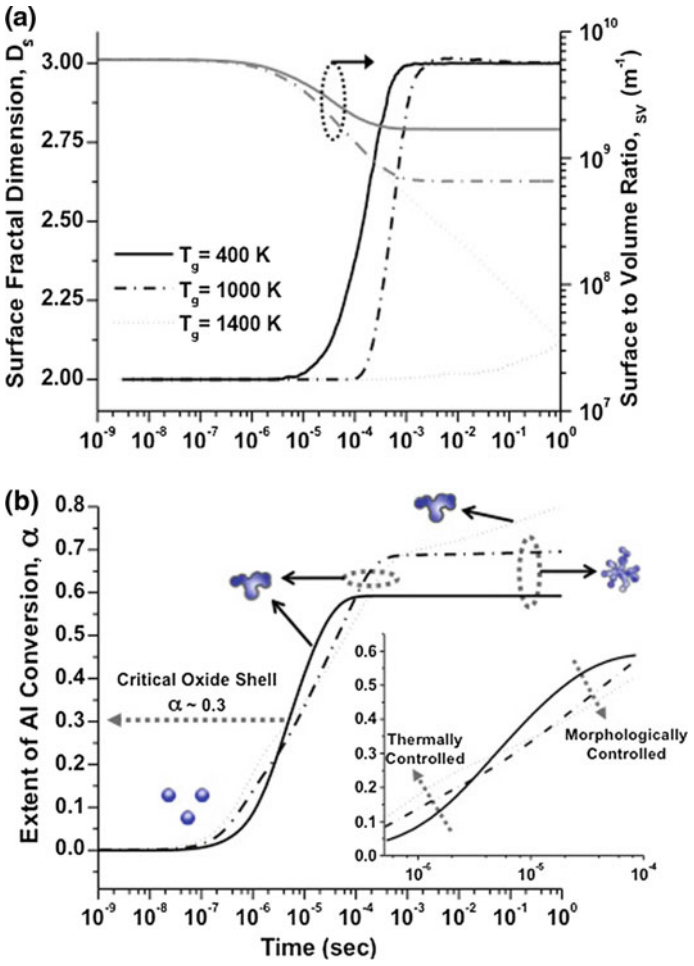

Fig. 22 Temporal variation of **a** surface fractal dimension, D_s (*black lines*; left y-axis); surface-to-volume ratio, ζ_{SV} (*gray lines*; right y-axis) and **b** extents of Al conversion, α in NPs synthesized at T_g = 400, 1000 and 1400 K (p_g = 1 atm and $\varphi = 10^{-6}$). Schematics indicate corresponding morphology during different stages of particle evolution (*Inset* Blow-up of α around the inflexion point, i.e., critical oxide shell, $\alpha \sim 0.3$)

already ensued (Fig. 22b). Eventually, while non-spherical particles ($D_s \sim 2$–2.5) attain the maximum α and fractal-like structures ($D_s = 3$) at later times ($>10^{-4}$ s) for T_g = 1000 K. In contrast, for T_g = 1400 K, the particles continue to exhibit a steady rise in α (Fig. 22b). The inflexion at $\alpha = 0.3$ (inset in Fig. 22b and prominent for T_g = 1400 K) separates the two energetic regimes: (1) thermally controlled oxidation prompting higher α with increasing T_g before the critical oxide shell formation and (2) morphologically controlled oxidation beyond this point, wherein non-spherical particles for T_g = 400 K (D_s = 2–2.5 from Fig. 22a

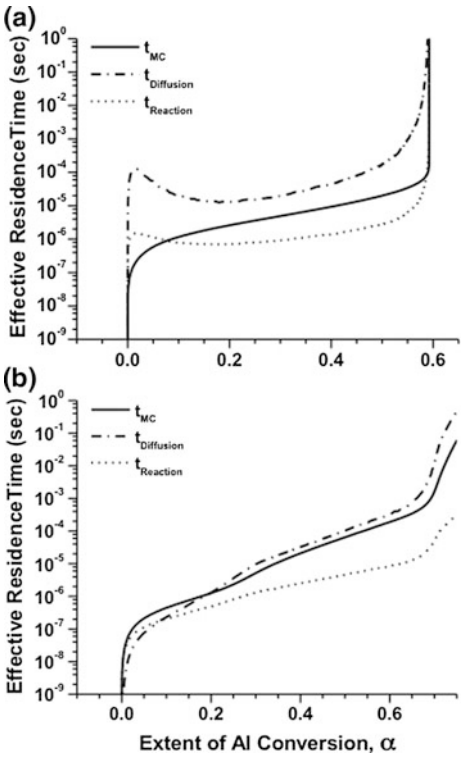

Fig. 23 Variation of theoretical residence times for reaction ($t_{Reaction}$) and diffusion ($t_{Diffusion}$) limited oxidation mechanisms as calculated from Eqs. (74a) and (74b) compared to the KMC simulation residence time (t_{MC}) as a function of extent of conversion α for: **a** T_g = 400 K and **b** T_g = 1400 K (p_g = 1 atm and $\varphi = 10^{-6}$)

and $<T_p> > 1000$ K from Fig. 21a) attain higher α than those for the other T_g ($D_s = 2$ till $\sim 10^{-4}$ s from Fig. 22a, while $<T_p> > 1200$ K from Fig. 21a). This is specifically exemplified by the T_g = 1400 K case (Fig. 22b).

To probe into the roles of classical oxidation mechanisms, Fig. 23 compares residence times from KMC simulations (t_{MC}) with those for typical reaction ($t_{Reaction}$) and diffusion ($t_{Diffusion}$) limited processes theoretically determined based on characteristic times for complete conversion via diffusion ($T_{Diffusion}$) or reaction ($T_{Reaction}$) as [150]:

$$\frac{t_{Reaction}}{T_{Reaction}} = 1 - (1-\alpha)^{1/3}; T_{Reaction} = \frac{\rho_{mol(Al)} d_p}{(8/3) k_f C_{O,\infty}} \tag{74a}$$

$$\frac{t_{Diffusion}}{T_{Diffusion}} = 1 - 3(1-\alpha)^{2/3} + 2(1-\alpha); T_{Diffusion} = \frac{\rho_{mol(Al)} d_p^2}{32 D_{O_2|Ash} C_{O,\infty}} \tag{74b}$$

where, $\rho_{mol(Al)}$ is the molar density of Al (mol m^{-3}). For T_g = 400 K, unlike common nanoparticle oxidation models [12, 139] the mechanism starts off as

reaction-limited but shifts between diffusion and reaction limited regimes (morphology controlled) as the particle evolves whereas for T_g = 1400 K, immediately after the initial oxide shell formation, t_{MC} uniformly follows the diffusion-limited mechanism trend (thermally activated with dominant coalescence) leading to continuous increase in α as discussed above.

Similar studies were also carried out for different background gas pressures (p_g) and volume loadings (ϕ). These studies also indicate the familiar bi-modal temperature profile depicting the energetic behavior of the fractal-like Al nanoparticles during their exothermic coalescence mediated surface oxidations. The energetic behavior for the aggregates were enhanced for lower gas pressure and lower volume loadings due to the lack of gas molecules to facilitate the heat dissipation from the nanoparticles in the former case, and the reduced collisions from lower particle concentrations promoting the exothermic coalescence in the latter. For further details on these studies, the readers can refer to Mukherjee et al. [49].

4.3.4 Implications of Coalescence-Driven Fractal like Morphology on the Surface Oxidation of Al/Al_2O_3 Nanoparticles

The unique contribution of the study presented here can be realized by comparing results for Al nanoparticle oxidation starting with an initial diameter, $d_{ini} \sim 1$ nm at T_g = 400 K and p_g = 1 atm while accounting for: (1) exothermic coalescence mediated morphological evolution of non-spherical nanoparticles generated via collision-coalescence mechanisms and (2) no morphological variations or, exothermic coalescence under the assumption of instant coalescence of colliding particles into spheres. As seen from Fig. 24a, b for T_g = 400 K, as particles in case 1 evolve from spherical shapes (D_s = 2) into fractal-like structures (D_s = 3), the extents of oxidation, α for case 1 is significantly higher than that for case 2 (black lines for case 1 and gray lines for case 2). In conjunction to this, final ζ_{SV} (Fig. 24b) for particles with complex morphology and larger surface area (case 1) is significantly higher than that for spherical particles (case 2), thereby supporting the enhanced α for case 1. Moreover, in case 1 the onset of fractal-like aggregates ($D_s > 2$ in Fig. 24a) generates particles with larger volume equivalent diameters $<d_{eq}>$ (Fig. 24b) as compared to their instantly coalesced spherical counterparts. It is noted that for case 1 significant amount of oxidation ($\alpha \sim 0.59$) ensues in the size regime of $<d_{eq}> <10$ nm ($t \sim 10^{-4}$ s.). Enhanced coalescence mediated thermal activities in spherical particles dominate the early stages till $<d_{eq}> \sim 1.5$ nm ($t \sim 4 \times 10^{-6}$ s) beyond which, until $<d_{eq}> \sim 10$ nm ($t \sim 10^{-4}$ s), coalescence mediated non-spherical morphology drives the final stages of particle oxidation, i.e., $\alpha \sim 0.3$–0.59 as $D_s \sim 2$–2.5 (as discussed earlier). In comparison, case 2 shows much slower and yet, continuous rise all through its evolution, irrespective of particle size or morphology.

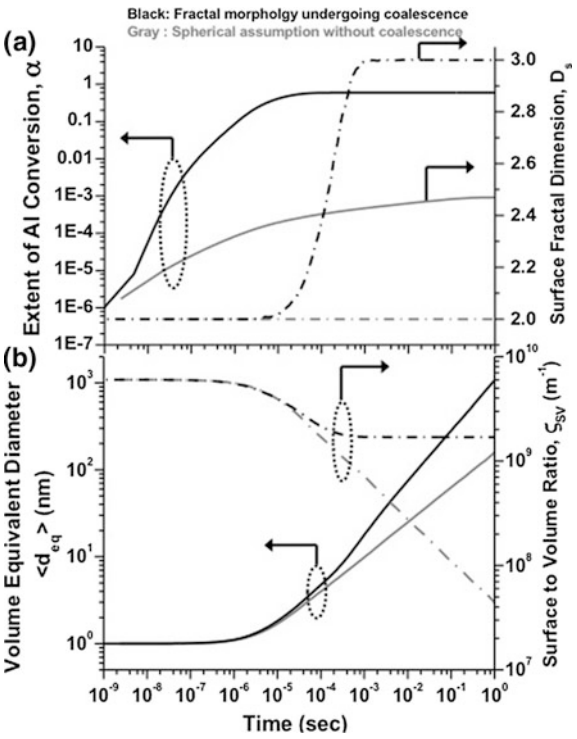

Fig. 24 KMC simulations comparing temporal variations of: **a** Extents of conversion, α (*solid lines* on left y-axis) and surface fractal dimension, Ds (*dash-dot lines* on right y-axis); **b** volume equivalent diameter, <deq> (*solid line* on left y-axis) and surface to volume ratio, ζ_{SV} (*dash-dot line* on right y-axis) (dini = 1 nm, Tg = 400 K, pg = 1 atm, and $\varphi = 10^{-6}$) for particles undergoing exothermic coalescence mediated morphological evolution (*all black lines*) and particles assumed to be spherical without any coalescence (*all gray line*)

5 Conclusion

In this chapter, we discussed the development of various computational models to study the fate, transport and evolution of metal NPs grown via aerosol routes. The results and discussions indicated the role of process parameters during gas-phase synthesis of metal NPs in tailoring their final sizes, shapes, compositions and structures, which, in turn, tune their surface reactivity and energetic behaviors. Homogeneous nucleation derived from CNT assumptions was introduced as the first step towards the inception of critical clusters as the new nanophase structures. Furthermore, a discussion on models that deviate from CNT was invoked that included the role of size-dependent surface tension as well as the breakdown of steady-state assumptions for small cluster sizes as revealed by our recently developed Gibbs' free energy-driven KMC model for vapor-phase nucleation studies. The sizes, shapes, and rates of formation of critical clusters determine the subsequent growth mechanisms, via surface growth and coagulation, for the seeding NPs.

We presented a KMC model that accounted for the ensemble effects of NP collision/coalescence phenomena, without any a priori constraint on the particle size distribution. The heat generation during typical non-isothermal coalescence phenomena was shown to bear a strong effect on the coalescing dynamics of metal

NPs that, in turn, played a significant role in dictating their final morphologies and sizes. Finally, the KMC model was further extended to study the effect of surface oxidation on the formation and growth of fractal-like nano-aggregates. These results elucidated the role of process parameters (background gas temperatures, gas pressures and particle volume loadings) in tailoring the energetic properties of metal/metal oxide nanostructures generated via gas phase synthesis. Specifically, results for non-isothermal coalescence in fractal-like particle morphology, when compared to those obtained with the assumption of instantly coalescing spherical particles clearly indicated the significant impact of the former case on surface oxidation of non-spherical metal NPs.

The computational studies consolidated in this chapter pave the path for our on-going efforts in developing a unified KMC-based model to simulate NP life-cycles from their inception to final growth and evolution into oxidized (surface passivated) fractal-like aggregates. Such studies will lay the foundation for fundamental theoretical understanding and, hitherto elusive comparisons with experimental results for the fate of metal NPs generated from vapor-phase synthesis.

Acknowledgements Figures, tables and discussions within Sects. 3 and 4 were in part or whole adapted/reprinted from the journal articles, *J. Chem. Phys. 119, 3391 (2003)* [44] and *AIChE J., 58,3341 (2012)* [49] with the author's (D. Mukherjee's) copyright permission from AIP publishing and Wiley Online respectively.

References

1. Renie J et al (1982) Aluminum particle combustion in composite solid propellants. Purdue University, West Lafayette, Ind
2. Bakhman N, Belyaev A, Kondrashkov YA (1970) Influence of the metal additives onto the burning rate of the model solid rocket propellants. Phys Combust Explos 6:93
3. Chiaverini MJ et al (1997) *Instantaneous regression behavior of HTPB solid fuels burning with GOX in a simulated hybrid rocket motor.* Int J Energ Mat Chem Propul 4(1–6)
4. Mench M, Yeh C, Kuo K (1998) Propellant burning rate enhancement and thermal behavior of ultra-fine aluminum powders(Alex). Energ Mat-Prod, Process Charac 30–1
5. Ritter H, Braun S (2001) High explosives containing ultrafine aluminum ALEX. Propellants, Explos, Pyrotech 26(6):311–314
6. Ilyin A et al (2002) Characterization of aluminum powders I. Parameters of reactivity of aluminum powders. Propellants Explos Pyrotech 27(6):361–364
7. Brousseau P, Anderson CJ (2002) Nanometric aluminum in explosives. Propellants, Explos, Pyrotech 27(5):300–306
8. Weiser V, Kelzenberg S, Eisenreich N (2001) Influence of the metal particle size on the ignition of energetic materials. Propellants, Explos, Pyrotech 26(6):284–289
9. Pantoya ML, Granier JJ (2005) Combustion behavior of highly energetic thermites: nano versus micron composites. Propellants, Explos, Pyrotech 30(1):53–62
10. Pivkina A et al (2004) Nanomaterials for heterogeneous combustion. Propellants, Explos, Pyrotech 29(1):39–48
11. van der Heijden AEDM et al (2006) Processing, application and characterization of (ultra) fine and nanometric materials in energetic compositions. Shock Compression Condens Matter Pts 1 and 2 845:1121–1126

12. Rai A et al (2006) Understanding the mechanism of aluminium nanoparticle oxidation. Combust Theor Model 10(5):843–859
13. Mason BA et al (2013) Combustion performance of several nanosilicon-based nanoenergetics. J Propul Power 29(6):1435–1444
14. Piekiel NW et al (2013) Combustion and material characterization of porous silicon nanoenergetics. In: 26th Ieee international conference on micro electro mechanical systems (Mems 2013) p 449–452
15. Thiruvengadathan R et al (2012) Combustion characteristics of silicon-based nanoenergetic formulations with reduced electrostatic discharge sensitivity. Propellants, Explos, Pyrotech 37(3):359–372
16. Prakash A, McCormick AV, Zachariah MR (2005) Synthesis and reactivity of a super-reactive metastable intermolecular composite formulation of Al/$KMnO_4$. Adv Mat 17(7):900–
17. Perry WL et al (2004) Nano-scale tungsten oxides for metastable intermolecular composites. Propellants, Explos, Pyrotech 29(2):99–105
18. Perry WL et al (2007) Energy release characteristics of the nanoscale aluminum-tungsten oxide hydrate metastable intermolecular composite. J Appl Phys 101(6)
19. Berner MK, Zarko VE, Talawar MB (2013) Nanoparticles of energetic materials: synthesis and properties (review). Combust Explosion Shock Waves 49(6):625–647
20. Prakash A, McCormick AV, Zachariah MR (2005) Tuning the reactivity of energetic nanoparticles by creation of a core-shell nanostructure. Nano Lett 5(7):1357–1360
21. Zhang KL et al (2007) Synthesis of large-area and aligned copper oxide nanowires from copper thin film on silicon substrate. Nanotechnology 18(27)
22. Prakash A, McCormick AV, Zachariah MR (2004) Aero-sol-gel synthesis of nanoporous iron-oxide particles: A potential oxidizer for nanoenergetic materials. Chem Mater 16 (8):1466–1471
23. Subramanian S et al (2008) Nanoporous silicon based energetic materials, DTIC Document
24. Blobaum KJ et al (2003) Deposition and characterization of a self-propagating CuO_x/Al thermite reaction in a multilayer foil geometry. J Appl Phys 94(5):2915–2922
25. Ma E et al (1990) Self-propagating explosive reactions in Al/Ni multilayer thin-films. Appl Phys Lett 57(12):1262–1264
26. Gen M, Ziskin M, Petrov I (1959) A study of the dispersion of aluminium aerosols as dependent on the conditions of their formation. Doklady Akademii Nauk SSSR 127(2):366–368
27. Kwon YS et al (2003) Passivation process for superfine aluminum powders obtained by electrical explosion of wires. Appl Surf Sci 211(1–4):57–67
28. Kwon YS et al (2007) Properties of powders produced by electrical explosions of copper-nickel alloy wires. Mater Lett 61(14–15):3247–3250
29. Sarathi R, Sindhu TK, Chakravarthy SR (2007) Generation of nano aluminium powder through wire explosion process and its characterization. Mater Charact 58(2):148–155
30. Tillotson TM et al (2001) Nanostructured energetic materials using sol-gel methodologies. J Non-Cryst Solids 285(1–3):338–345
31. Jacobson MZ, Turco RP (1995) Simulating condensational growth, evaporation, and coagulation of aerosols using a combined moving and stationary size grid. Aerosol Sci Technol 22(1):73–92
32. Biswas P et al (1997) Characterization of iron oxide-silica nanocomposites in flames. 2. Comparison of discrete-sectional model predictions to experimental data. J Mater Res 12 (3):714–723
33. Landgrebe JD, Pratsinis SE (1990) A discrete-sectional model for particulate production by gas-phase chemical-reaction and aerosol coagulation in the free-molecular regime. J Colloid Interface Sci 139(1):63–86
34. Lehtinen KEJ, Zachariah MR (2001) Self-preserving theory for the volume distribution of particles undergoing Brownian coagulation. J Colloid Interface Sci 242(2):314–318
35. Girshick SL, Chiu CP (1989) homogeneous nucleation of particles from the vapor-phase in thermal plasma synthesis. Plasma Chem Plasma Process 9(3):355–369

36. Panda S, Pratsinis SE (1995) Modeling the synthesis of aluminum particles by evaporation-condensation in an aerosol flow reactor. Nanostruct Mater 5(7–8):755–767
37. Prakash A, Bapat AP, Zachariah MR (2003) A simple numerical algorithm and software for solution of nucleation, surface growth, and coagulation problems. Aerosol Sci Technol 37(11):892–898
38. Mukherjee D, Prakash A, Zachariah MR (2006) Implementation of a discrete nodal model to probe the effect of size-dependent surface tension on nanoparticle formation and growth. J Aerosol Sci 37(10):1388–1399
39. Zachariah MR, Carrier MJ (1999) Molecular dynamics computation of gas-phase nanoparticle sintering: a comparison with phenomenological models. J Aerosol Sci 30 (9):1139–1151
40. Yasuoka K, Matsumoto M (1998) Molecular dynamics of homogeneous nucleation in the vapor phase. I. Lennard-Jones fluid. J Chem Phys 109(19):8451–8462
41. Lummen N, Kraska T (2005) Molecular dynamics investigation of homogeneous nucleation and cluster growth of platinum clusters from supersaturated vapour. Nanotechnology 16 (12):2870–2877
42. Li ZH et al (2007) Free energies of formation of metal clusters and nanoparticles from molecular simulations: Al-n with n = 2–60. J Phys Chem C 111(44):16227–16242
43. McGreevy RL (2001) Reverse Monte Carlo modelling. J Phys-Condens Matter 13(46): R877–R913
44. Mukherjee D, Sonwane CG, Zachariah MR (2003) Kinetic Monte Carlo simulation of the effect of coalescence energy release on the size and shape evolution of nanoparticles grown as an aerosol. J Chem Phys 119(6):3391–3404
45. Gillespie DT (1975) Exact method for numerically simulating stochastic coalescence process in a cloud. J Atmos Sci 32(10):1977–1989
46. Liffman K (1992) A direct simulation Monte-Carlo method for cluster coagulation. J Comput Phys 100(1):116–127
47. Kruis FE, Maisels A, Fissan H (2000) Direct simulation Monte Carlo method for particle coagulation and aggregation. AIChE J 46(9):1735–1742
48. Efendiev Y, Zachariah MR (2002) Hybrid Monte Carlo method for simulation of two-component aerosol coagulation and phase segregation. J Colloid Interface Sci 249(1):30–43
49. Mukherjee D, Wang M, Khomami B (2012) Impact of particle morphology on surface oxidation of nanoparticles: a kinetic Monte Carlo based study. AIChE J 58(11):3341–3353
50. Auer S, Frenkel D (2001) Prediction of absolute crystal-nucleation rate in hard-sphere colloids. Nature 409(6823):1020–1023
51. Valeriani C et al (2007) Computing stationary distributions in equilibrium and nonequilibrium systems with forward flux sampling. J Chem Phys 127(11)
52. Allen RJ, Valeriani C, Ten Wolde PR (2009) Forward flux sampling for rare event simulations. J Phys-Condens Matter 21(46)
53. Katz JL et al (1976) Condensation of a supersaturated vapor. III. The homogeneous nucleation of CCl4, CHCl3, CCl_3F, and $C_2H_2C_{l4}$. J Chem Phys 65(1):382–392
54. Katz JL (1970) Condensation of a Supersaturated Vapor. I. The homogeneous nucleation of the *n*-alkanes. J Chem Phys 52(9):4733–4748
55. Oxtoby DW (1992) Homogeneous nucleation: theory and experiment. J Phys: Condens Matter 4(38):7627
56. Rusyniak M et al (2001) Vapor phase homogeneous nucleation of higher alkanes: dodecane, hexadecane, and octadecane. 1. Critical supersaturation and nucleation rate measurements. J Phys Chem B 105(47):11866–11872
57. Finney EE, Finke RG (2008) Nanocluster nucleation and growth kinetic and mechanistic studies: a review emphasizing transition-metal nanoclusters. J Colloid Interface Sci 317(2):351–374
58. Schmitt JL (1981) Precision expansion cloud chamber for homogeneous nucleation studies. Rev Sci Instrum 52(11):1749–1754

59. Wagner P, Strey R (1981) Homogeneous nucleation rates of water vapor measured in a two-piston expansion chamber. J Phys Chem 85(18):2694–2698
60. Hameri K, Kulmala M (1996) Homogeneous nucleation in a laminar flow diffusion chamber: the effect of temperature and carrier gas on dibutyl phthalate vapor nucleation rate at high supersaturations. J Chem Phys 105(17):7696–7704
61. Anisimov MP, Hameri K, Kulmala M (1994) Construction and test of laminar-flow diffusion chamber–homogeneous nucleation of Dbp and *N*-hexanol. J Aerosol Sci 25(1):23–32
62. Wyslouzil BE et al (1991) Binary nucleation in acid water-systems. 2. Sulfuric-acid water and a comparison with methanesulfonic-acid water. J Chem Phys 94(10):6842–6850
63. Viisanen Y, Kulmala M, Laaksonen A (1997) Experiments on gas-liquid nucleation of sulfuric acid and wafer. J Chem Phys 107(3):920–926
64. Fisk JA et al (1998) The homogeneous nucleation of cesium vapor. Atmos Res 46 (3–4):211–222
65. Ferguson FT, Nuth JA (2000) Experimental studies of the vapor phase nucleation of refractory compounds. V. The condensation of lithium. J Chem Phys 113(10):4093–4102
66. Zhang RY et al (2012) Nucleation and growth of nanoparticles in the atmosphere. Chem Rev 112(3):1957–2011
67. Lu HM, Jiang Q (2005) Size-dependent surface tension and Tolman's length of droplets. Langmuir 21(2):779–781
68. Lai SL et al (1996) Size-dependent melting properties of small tin particles: nanocalorimetric measurements. Phys Rev Lett 77(1):99–102
69. Tomanek D, Schluter MA (1986) Calculation of magic numbers and the stability of small Si clusters. Phys Rev Lett 56(10):1055–1058
70. Boustani I et al (1987) Systematic ab initio configuration-interaction study of alkali-metal clusters: Relation between electronic structure and geometry of small Li clusters. Phys Rev B 35(18):9437
71. Li ZH, Truhlar DG (2008) Cluster and nanoparticle condensation and evaporation reactions. Thermal rate constants and equilibrium constants of Al(m) + Al(n−m) <-> Al(n) with n = 2–60 and m = 1–8. J Phys Chem C 112(30):11109–11121
72. Girshick SL, Agarwal P, Truhlar DG (2009) Homogeneous nucleation with magic numbers: aluminum. J Chem Phys 131(13)
73. Wyslouzil BE, Seinfeld JH (1992) Nonisothermal homogeneous nucleation. J Chem Phys 97 (4):2661–2670
74. Barrett JC (2008) A stochastic simulation of nonisothermal nucleation. J Chem Phys 128(16)
75. Domilovsky ER, Lushnikov AA, Piskunov VN (1979) Monte-Carlo simulation of coagulation processes. Izvestiya Akademii Nauk Sssr Fizika Atmosfery I Okeana 15 (2):194–201
76. Debry E, Sportisse B, Jourdain B (2003) A stochastic approach for the numerical simulation of the general dynamics equation for aerosols. J Comput Phys 184(2):649–669
77. Garcia A et al (1987) A Monte Carlo method of coagulation. Phys A 143:535–546
78. Smith M, Matsoukas T (1998) Constant-number Monte Carlo simulation of population balances. Chem Eng Sci 53(9):1777–1786
79. Efendiev Y, Zachariah MR (2003) Hierarchical hybrid Monte-Carlo method for simulation of two-component aerosol nucleation, coagulation and phase segregation. J Aerosol Sci 34(2):169–188
80. Davari SA, Mukherjee D (2017) Kinetic Monte Carlo simulation for homogeneous nucleation of metal nanoparticles during vapor phase synthesis. AIChE J. Accepted. doi:10.1002/aic.15887
81. Pratsinis SE (1998) Flame aerosol synthesis of ceramic powders. Prog Energy Combust Sci 24(3):197–219
82. Mench MM et al (1998) Comparison of thermal behavior of regular and ultra-fine aluminum powders (Alex) made from plasma explosion process. Combust Sci Technol 135(1–6):269–292
83. Ozaki Y, Ichinose N, Kashū S (1992) Superfine particle technology. Springer, Berlin

84. Megaridis CM, Dobbins RA (1990) Morphological description of flame-generated materials. Combust Sci Technol 71(1–3):95–109
85. Friedlander SK (1977) Smoke, dust and haze: Fundamentals of aerosol behavior. Wiley-Interscience, New York, vol 333, p 1
86. Lehtinen KEJ, Zachariah MR (2001) Effect of coalescence energy release on the temporal shape evolution of nanoparticles. Phys Rev B 63(20)
87. Windeler RS, Lehtinen KEJ, Friedlander SK (1997) Production of nanometer-sized metal oxide particles by gas phase reaction in a free jet. 2. Particle size and neck formation - Comparison with theory. Aerosol Sci Technol 27(2):191–205
88. Windeler RS, Friedlander SK, Lehtinen KEJ (1997) Production of nanometer-sized metal oxide particles by gas phase reaction in a free jet. 1. Experimental system and results. Aerosol Sci Technol 27(2):174–190
89. Tsantilis S, Pratsinis SE (2000) Evolution of primary and aggregate particle-size distributions by coagulation and sintering. AIChE J 46(2):407–415
90. Ehrman SH, Friedlander SK, Zachariah MR (1998) Characteristics of SiO_2/TiO_2 nanocomposite particles formed in a premixed flat flame. J Aerosol Sci 29(5–6):687–706
91. Schweigert IV et al (2002) Structure and properties of silica nanoclusters at high temperatures. Phys Rev B 65(23)
92. Kruis FE et al (1993) A simple-model for the evolution of the characteristics of aggregate particles undergoing coagulation and sintering. Aerosol Sci Technol 19(4):514–526
93. Xing YC, Rosner DE (1999) Prediction of spherule size in gas phase nanoparticle synthesis. J Nanopart Res 1(2):277–291
94. Freund HJ, Bauer SH (1977) Homogeneous nucleation in metal vapors. 2. Dependence of heat of condensation on cluster size. J Phys Chem 81(10):994–1000
95. Lehtinen K, Zachariah M (2001) Energy accumulation during the coalescence and coagulation of nanoparticles. Phys Rev B 63(20):205402
96. Zachariah MR, Carrier MJ, BlaistenBarojas E (1996) Properties of silicon nanoparticles: a molecular dynamics study. J Phys Chem 100(36):14856–14864
97. Koch W, Friedlander SK (1990) The effect of particle coalescence on the surface-area of a coagulating aerosol. J Colloid Interface Sci 140(2):419–427
98. Wu MK et al (1993) Controlled synthesis of nanosized particles by aerosol processes. Aerosol Sci Technol 19(4):527–548
99. Martin DL, Raff LM, Thompson DL (1990) Silicon dimer formation by three-body recombination. J Chem Phys 92(9):5311–5318
100. Yaws C (1994) Handbook of vapor pressure. Gulf Pub. Co., Houston
101. Buffat P, Borel JP (1976) Size effect on the melting temperature of gold particles. Phys Rev A 13(6):2287
102. Tandon P, Rosner DE (1999) Monte Carlo simulation of particle aggregation and simultaneous restructuring. J Colloid Interface Sci 213(2):273–286
103. Iida T et al (2000) Equation for estimating viscosities of industrial mold fluxes. High Temp Mater Processes (London) 19(3–4):153–164
104. Hansen K, Campbell EEB (1998) Thermal radiation from small particles. Phys Rev E 58 (5):5477–5482
105. Kumar S, Tien CL (1990) Dependent absorption and extinction of radiation by small particles. J Heat Transfer-Trans Asme 112(1):178–185
106. Tomchuk PM, Tomchuk BP (1997) Optical absorption by small metallic particles. J Exp Theor Phys 85(2):360–369
107. Altman IS et al (2001) Experimental estimate of energy accommodation coefficient at high temperatures. Phys Rev E 64(5)
108. Bohren CF, Huffman DR (1983) Absorption and scattering by a sphere. Absorption Scattering Light Small Part 82–129
109. Siegel R, Howel J (1992) Thermal radiation heat transfer. Hemisphere Publishing Corp, Washington DC

110. Rosner DE, Yu SY (2001) MC simulation of aerosol aggregation and simultaneous spheroidization. AIChE J 47(3):545–561
111. Norris JR (1999) Smoluchowski's coagulation equation: uniqueness, nonuniqueness and a hydrodynamic limit for the stochastic coalescent. Ann Appl Probab 9(1):78–109
112. Kostoglou M, Konstandopoulos AG (2001) Evolution of aggregate size and fractal dimension during Brownian coagulation. J Aerosol Sci 32(12):1399–1420
113. Gooch JRV, Hounslow MJ (1996) Monte Carlo simulation of size-enlargement mechanisms in crystallization. AIChE J 42(7):1864–1874
114. Shah BH, Ramkrishna D, Borwanker JD (1977) Simulation of particulate systems using concept of interval of quiescence. AIChE J 23(6):897–904
115. Friedlander SK, Wu MK (1994) Linear rate law for the decay of the excess surface-area of a coalescing solid particle. Phys Rev B 49(5):3622–3624
116. Vemury S, Kusters KA, Pratsinis SE (1994) Time-lag for attainment of the self-preserving particle-size distribution by coagulation. J Colloid Interface Sci 165(1):53–59
117. Rosner DE (2005) Flame synthesis of valuable nanoparticles: Recent progress/current needs in areas of rate laws, population dynamics, and characterization. Ind Eng Chem Res 44 (16):6045–6055
118. Strobel R, Pratsinis SE (2007) Flame aerosol synthesis of smart nanostructured materials. J Mater Chem 17(45):4743–4756
119. Bapat A et al (2004) Plasma synthesis of single-crystal silicon nanoparticles for novel electronic device applications. Plasma Phys Controlled Fusion 46:B97–B109
120. Holunga DM, Flagan RC, Atwater HA (2005) A scalable turbulent mixing aerosol reactor for oxide-coated silicon nanoparticles. Ind Eng Chem Res 44(16):6332–6341
121. Kommu S, Wilson GM, Khomami B (2000) A theoretical/experimental study of silicon epitaxy in horizontal single-wafer chemical vapor deposition reactors. J Electrochem Soc 147(4):1538–1550
122. Gelbard F, Tambour Y, Seinfeld JH (1980) Sectional representations for simulating aerosol dynamics. J Colloid Interface Sci 76(2):541–556
123. Frenklach M, Harris SJ (1987) Aerosol dynamics modeling using the method of moments. J Colloid Interface Sci 118(1):252–261
124. Whitby ER, McMurry PH (1997) Modal aerosol dynamics modeling. Aerosol Sci Technol 27(6):673–688
125. Kommu S, Khomami B, Biswas P (2004) Simulation of aerosol dynamics and transport in chemically reacting particulate matter laden flows. Part I: algorithm development and validation. Chem Eng Sci 59(2):345–358
126. Garrick SC, Lehtinen KEJ, Zachariah MR (2006) Nanoparticle coagulation via a Navier-Stokes/nodal methodology: Evolution of the particle field. J Aerosol Sci 37(5):555–576
127. Tsantilis S, Pratsinis SE (2004) Soft- and hard-agglomerate aerosols made at high temperatures. Langmuir 20(14):5933–5939
128. Wu MK, Friedlander SK (1993) Enhanced power-law agglomerate growth in the free-molecule regime. J Aerosol Sci 24(3):273–282
129. Maricq MM (2007) Coagulation dynamics of fractal-like soot aggregates. J Aerosol Sci 38(2):141–156
130. Zurita-Gotor M, Rosner DE (2002) Effective diameters for collisions of fractal-like aggregates: Recommendations for improved aerosol coagulation frequency predictions. J Colloid Interface Sci 255(1):10–26
131. Schmid HJ et al (2006) Evolution of the fractal dimension for simultaneous coagulation and sintering. Chem Eng Sci 61(1):293–305
132. Zhou L et al (2008) Ion-mobility spectrometry of nickel nanoparticle oxidation kinetics: application to energetic materials. J Phys Chem C 112(42):16209–16218
133. Dikici B et al (2009) Influence of aluminum passivation on the reaction mechanism: flame propagation studies. Energy Fuels 23:4231–4235
134. Wang CM et al (2009) Morphology and electronic structure of the oxide shell on the surface of iron nanoparticles. J Am Chem Soc 131(25):8824–8832

135. Rai A et al (2004) Importance of phase change of aluminum in oxidation of aluminum nanoparticles. J Phys Chem B 108(39):14793–14795
136. Sun J, Pantoya ML, Simon SL (2006) Dependence of size and size distribution on reactivity of aluminum nanoparticles in reactions with oxygen and MoO3. Thermochim Acta 444(2):117–127
137. Trunov MA et al (2005) Effect of polymorphic phase transformations in Al_2O_3 film on oxidation kinetics of aluminum powders. Combust Flame 140(4):310–318
138. Aumann CE, Skofronick GL, Martin JA (1995) Oxidation behavior of aluminum nanopowders. J Vac Sci Technol, B 13(3):1178–1183
139. Park K et al (2005) Size-resolved kinetic measurements of aluminum nanoparticle oxidation with single particle mass spectrometry. J Phys Chem B 109(15):7290–7299
140. Mukherjee D, Rai A, Zachariah MR (2006) Quantitative laser-induced breakdown spectroscopy for aerosols via internal calibration: application to the oxidative coating of aluminum nanoparticles. J Aerosol Sci 37(6):677–695
141. Alavi S, Mintmire JW, Thompson DL (2005) Molecular dynamics simulations of the oxidation of aluminum nanoparticles. J Phy Chem B 109(1):209–214
142. Vashishta P, Kalia RK, Nakano A (2006) Multimillion atom simulations of dynamics of oxidation of an aluminum nanoparticle and nanoindentation on ceramics. J Phys Chem B 110(8):3727–3733
143. Zhang F, Gerrard K, Ripley RC (2009) Reaction mechanism of aluminum-particle-air detonation. J Propul Power 25(4):845–858
144. Trunov MA et al (2006) Oxidation and melting of aluminum nanopowders. J Phys Chem B 110(26):13094–13099
145. Xiong Y, Pratsinis SE (1993) Formation of agglomerate particles by coagulation and sintering. 1. A 2-dimensional solution of the population balance equation. J Aerosol Sci 24(3):283–300
146. Mandelbrot BB (1983) The fractal geometry of nature 173 (Macmillan)
147. Meakin P, Witten TA (1983) Growing interface in diffusion-limited aggregation. Phys Rev A 28(5):2985–2989
148. Schmidtott A (1988) New approaches to insitu characterization of ultrafine agglomerates. J Aerosol Sci 19(5):553–563
149. Buffat P, Borel JP (1976) Size effect on melting temperature of gold particles. Phys Rev A 13(6):2287–2298
150. Levenspiel O (1999) Chemical reaction engineering. Ind Eng Chem Res 38(11):4140–4143
151. German RM (1996) Sintering theory and practice. Wiley, New York
152. Assael MJ et al (2006) Reference data for the density and viscosity of liquid aluminum and liquid iron. J Phys Chem Ref Data 35(1):285–300
153. Paradis P-F, Ishikawa T (2005) Surface tension and viscosity measurements of liquid and undercooled alumina by containerless techniques. Jpn J Appl Phys 44:5082–5085
154. Sarou-Kanian V, Millot F, Rifflet JC (2003) Surface tension and density of oxygen-free liquid aluminum at high temperature. Int J Thermophys 24(1):277–286
155. Blackburn PE, Buchler A, Stauffer JL (1966) Thermodynamics of vaporization in the aluminum oxide-boron oxide system. J Phys Chem 70(8):2469–2474
156. Polyak EV, Sergeev SV (1941) Compt Rend (Doklady) Acad Sci URSS 33
157. Samsonov G (1982) The oxide handbook. Springer, New York
158. Jensen JE et al (1980) Brookhaven national laboratory selected cryogenic data notebook, U. S.D.O.E. Brookhaven National Laboratory Associated Universities Inc., Editor. Brookhaven national Laboratory Associated Universities: UptUUpton, NY
159. Munro RG (1997) Evaluated material properties for a sintered alpha-alumina. J Am Ceram Soc 80(8):1919–1928
160 Weast RC (1989) CRC handbook of chemistry and physics. CRC Press, Boca Raton, FL
161 Astier M, Vergnon P (1976) Determination of the diffusion coefficients from sintering data of ultrafine oxide particles. J Solid State Chem 19(1):67–73